Post-stroke epileptogenesis is associated with altered intrinsic properties of hippocampal pyramidal neurons leading to increased theta resonance

Jorge Vera [a,b,1], Kristina Lippmann [a,c,*,1]

[a] *Grass Laboratory, Marine Biological Laboratory, Woods Hole, MA 02543, USA*
[b] *Dominick P. Purpura Department of Neuroscience, Albert Einstein College of Medicine, Bronx, NY 10461, USA*
[c] *Carl-Ludwig-Institute for Physiology, Medical Faculty, University of Leipzig, D-04103 Leipzig, Germany*

ARTICLE INFO

ABSTRACT

Brain insults like stroke, trauma or infections often lead to blood-brain barrier-dysfunction (BBBd) frequently resulting into epileptogenesis. Affected patients suffer from seizures and cognitive comorbidities that are potentially linked to altered network oscillations. It has been shown that a hippocampal BBBd in rats leads to in vivo seizures and increased power at theta (3–8 Hz), an important type of network oscillations. However, the underlying cellular mechanisms remain poorly understood. At membrane potentials close to the threshold for action potentials (APs) a subpopulation of CA1 pyramidal cells (PCs) displays intrinsic resonant properties due to an interplay of the muscarine-sensitive K^+-current (I_M) and the persistent Na^+-current (I_{NaP}). Such resonant neurons are more excitable and generate more APs when stimulated at theta frequencies, being strong candidates for contributing to hippocampal theta oscillations during epileptogenesis. We tested this hypothesis by characterizing changes in intrinsic properties of hippocampal PCs one week after post-stroke epileptogenesis, a model associated with BBBd, using slice electrophysiology and computer modeling. We find a higher proportion of resonant neurons in BBBd compared to sham animals (47 vs. 29%), accompanied by an increase in their excitability. In contrast, BBBd non-resonant neurons showed a reduced excitability, presented with lower impedance and more positive AP threshold. We identify an increase in I_M combined with either a reduction in I_{NaP} or an increase in I_{Leak} as possible mechanisms underlying the observed changes. Our results support the hypothesis that a higher proportion of more excitable resonant neurons in the hippocampus contributes to increased theta oscillations and an increased likelihood of seizures in a model of post-stroke epileptogenesis.

1. Introduction

Epileptogenesis, the process in which an impaired brain becomes epileptic, is the time period for preventing disease progress into epilepsy. In fact, an effective disease prevention requires the understanding of the underlying pathophysiological mechanisms. Previously, it has been shown that specific alterations in the neuronal network activity are frequently observed during epileptogenesis. These include changes in the power of gamma and theta oscillations as well as in sharp-wave ripples that are most prominent in the hippocampal formation, an area important for learning and memory and prone to develop epileptic

activity (Buzsáki, 2015; Noebels et al., 2012; Valero et al., 2017). Theta oscillations (3–8 Hz), one type of brain network oscillations particular important for episodic memory as well as spatial and temporal information processing (Buzsáki, 2002), appears to be increased in a model of acquired epileptogenesis. In this model, local field potential recordings of hippocampal activity in behaving rats undergoing epileptogenesis show a larger power in theta oscillations together (Lippmann et al., 2017) with hyperexcitability compared to sham rats (Lapilover et al., 2012; Lippmann et al., 2017). These changes of hippocampal activity suggest that epileptogenesis is boosting the mechanisms underlying theta oscillations. As of today, the cellular alterations underlying these

changes in network activity are poorly understood.

Hippocampal theta oscillations are generated from the interplay of synaptic and intrinsic membrane properties that are tuned to favor synaptic transmission, signal integration and action potential (AP) generation at theta frequencies (Buzsáki, 2002). Potentially important for the generation of theta activity is the fact that CA1 pyramidal cells (PCs) behave as resonators, displaying higher voltage responses for inputs at theta frequencies (Hu et al., 2002; Hutcheon and Yarom, 2000). While all PCs display resonance at hyperpolarized potential (Hu et al., 2002), only a subpopulation (~20%) displays resonance at near-threshold (perithreshold) potential (Vera et al., 2017) and, thereby, is able to generate APs at theta frequencies as well as to communicate the preferred theta frequency to downstream neurons (Richardson et al., 2003; Rotstein, 2014; Vera et al., 2020). Therefore, resonant neurons are likely to contribute to increased theta power that was observed together with hippocampal epileptic activity in vivo (Lippmann et al., 2017).

This perithreshold theta resonance is mediated by the interplay of muscarine-sensitive potassium current (I_M), leak current (I_{Leak}) and the persistent sodium current (I_{NaP}) (Vera et al., 2017). All PCs contain I_M, I_{Leak} and I_{NaP}, but whether they express perithreshold resonance depends on the resulting amplitude of those currents. Neurons containing high levels of I_{NaP} and low levels of I_M and I_{Leak} are highly excitable and depolarize too fast to allow I_M to become activated, therefore those neurons are not expressing resonance ('NonRes' neurons). In contrast, neurons that are able to activate I_M and I_{Leak} below threshold express perithreshold resonance and increase AP firing probability at theta frequencies ('Res' neurons) (Vera et al., 2017). As I_M, I_{Leak} and I_{NaP} are highly modulated by metabotropic signaling (Astman et al., 1998; Delmas and Brown, 2005; Gorelova and Yang, 2000; Mantegazza et al., 2005; Moore et al., 1988; Schweitzer, 2000), and cholinergic neuromodulation (Halliwell and Adams, 1982; Madison et al., 1987; Yamada-Hanff and Bean, 2013), it is possible that the fraction of resonant neurons changes dynamically (Vera et al., 2017). Moreover, it has been described that epileptogenesis homeostatically downregulates the cholinergic system (Friedman et al., 2007; Gnatek et al., 2012), suggesting that perithreshold resonance could therewith be strongly influenced.

Here we use in vitro electrophysiology as well as computer simulations to test whether epileptogenesis is associated with changes in resonant proportion and properties of PCs. We studied this question in a model of blood-brain barrier-dysfunction (BBBd) in the rat hippocampus, because BBBd represents a common cause for acquired epileptogenesis after brain diseases like stroke, tumor, trauma or infections (Abbott et al., 2006; Neuwelt, 2004). Indeed, we find that following a cortical stroke the hippocampal area CA1 is characterized by containing a higher proportion of resonant neurons and, in addition, by resonant cells showing a higher and non-resonant cells showing a lower excitability compared to sham conditions.

2. Materials and methods

2.1. Ethics

The Institutional Animal Care & Use Committee of the Marine Biological Laboratory, Woods Hole, MA, USA, approved the animal care and experimental procedures under the protocol number 17-07C according to the applicable U.S. *Animal Welfare Act*. By combining experiments including perioperative analgesia and computer simulations we followed the 3R guidelines in animal research (Replacement, Reduction, Refinement).

2.2. Photothrombotic stroke induction

A photothrombotic stroke or sham surgery was performed on male adult Sprague Dawley rats (9–12 weeks old), as previously described (Lippmann et al., 2017). In short, rats were anesthetized via an intraperitoneal injection of ketamine and xylazine (100 and 10 mg/kg body weight (b.w.), respectively). Animals were preemptively treated with the analgesics metamizole [100 mg/kg b.w. injected subcutaneously (s.c.)] and lidocaine (2% gel on the scalp). Body temperature was rectally monitored and kept constant at 37 °C via an electronically controlled heating pad. Rats were head fixed in a stereotactic frame, the scalp was incised and the right calvarium was exposed to a light guide (∅ = 3.5 mm, which was centered 2.75 mm posterior and 2.75 mm lateral from bregma). Either the photosensitizer Rose bengal (20 mg/kg b.w., dissolved in saline, animal $n = 5$) or saline alone (animal $n = 3$) was injected intravenously into the tail vein, for stroke induction or sham condition, respectively. After the skull was illuminated for 15 min (150 W halogen lamp, Zeiss KL 1500 LCD, 3E) the scalp was sutured, and a depot of saline was injected s.c. (15 ml/kg b.w.). Postoperative analgesia was supplied via the drinking water for 2 days (400 mg metamizole +4 ml 20% glucose per 100 ml water) and animal health was checked daily.

2.3. Slice preparation

One week after surgery, rats were deeply anesthetized using ketamine/xylazine as described above. Rats were transcardially perfused with an ice-cold dissection solution containing (in mM): 206 sucrose, 2.8 KCl, 1 MgCl₂, 2 MgSO₄, 1 CaCl₂, 26 NaHCO₃, 1.125 NaH₂PO₄, 10 glucose and 0.4 ascorbic acid (equilibrated with 95% O₂ and 5% CO₂), pH 7.3 (Vera et al., 2017) for at least 2 min until the blood was fully exchanged with the dissecting solution. Rats were then decapitated and their brain was rapidly removed and transferred into the same solution. Parasagittal cortico-hippocampal slices of the treated (i.e., the right) hemisphere, containing the dorsal hippocampus, were obtained using a vibratome (Leica VT1000S). Slices were transferred to a submerged holding chamber filled with artificial cerebro-spinal fluid (ACSF) containing (in mM): 124 NaCl, 2.8 KCl, 1.25 NaH₂PO₄, 26 NaHCO₃, 10 Glucose, 2 MgCl₂, 2 CaCl₂ and 0.4 ascorbic acid (equilibrated with 95% O2 and 5% CO2), adjusted to pH 7.3 and 290 mOsm. Slices were allowed to recover for at least 1 h at room temperature before using them for recordings. Brains for the BBBd group were visually checked for a sufficient photothrombosis through all cortical layers before taking brains into account for the treatment group to ensure a hippocampal BBBd as shown in several of our previous publications (Kim et al., 2017; Lapilover et al., 2012; Lippmann et al., 2017).

2.4. Electrophysiological recordings

The experimental procedure was previously described (Vera et al., 2020; Vera et al., 2017). For this study, 17 neurons were recorded from 3 sham-treated animals and 19 neurons were recorded from 5 BBBd-treated animals. In short, whole cell patch clamp recordings of CA1 pyramidal cells were conducted at 34 ± 2 °C under visual guidance using an upright microscope (Axio Examiner.A1, Zeiss, Germany) equipped with DIC optics. Neurons were recorded from the medial CA1 region of the dorsal hippocampus that is particularly affected from BBBd (Lippmann et al., 2017). Patch pipettes were fabricated from borosilicate glass using a horizontal puller (Model P-1000, Sutter Instruments, USA). Voltage-clamp recordings (acquisition rate 40 kHz, filtered at 10 kHz) were performed with a DOUBLE IPA amplifier and the SutterPatch software (Sutter Instruments, USA). The series resistance was constantly monitored and compensated up to 60–70% in order to keep the effective series resistance constant. The liquid junction potential was measured between pipette solution and ACSF according to the procedure described elsewhere (Neher, 1992), and recorded values (12 mV) were corrected offline during analyses. Experiments were conducted in the presence of 10 μM CNQX and 100 μM PTX (Tocris Bioscience, UK) to block AMPA and GABA_A receptors, respectively. Internal pipette solution contained (in mM): 123 K-Gluconate, 10 KCl, 4 Glucose, 1 EGTA, 10 HEPES, 2 Na₂ATP, 0.2 Na₃GTP, 10 phosphocreatine-Na, 1 MgCl₂, 0.1 CaCl₂, pH 7.35 and 290 mOsm (Vera et al., 2020).

2.5. ZAP stimulation and data analysis

The ZAP (impedance amplitude profile) stimulus consisted of a pseudo-sinusoidal current of constant amplitude and linearly increasing frequency from 0 to 20 Hz in 10 s (Puil et al., 1986). The protocol was repeated 8 to 10 times in every neuron and the membrane voltage responses were averaged for the impedance analysis. The impedance profile [Z(f)] was obtained from the ratio of the Fast Fourier Transforms (FFT) of the output (voltage) and input (current) waves (Z(f) = FFT[V(t)]/FFT[I(t)]). The impedance is a complex quantity [Z(f) = Z_{Real} + i$Z_{Imaginary}$], where Z_{Real} is the resistive component of the impedance and $Z_{Imaginary}$ the reactive component. For a given frequency, the complex impedance can be plotted as a vector, whose magnitude and phase lag [Φ(f), i.e., the angle with the real axis], respectively, are given by the following expressions:

$$|Z|(f) = \sqrt{Z_{Real}^2(f) + Z_{Imaginary}^2(f)} \tag{1}$$

$$\Phi(f) = \tan^{-1}\left(\frac{Z_{Imaginary}(f)}{Z_{Real}(f)}\right) \tag{2}$$

Throughout the text, the term 'impedance' refers to the magnitude of the impedance vector. The impedance 'phase lag' corresponds to the phase shift of the voltage wave relative to the current wave. Frequencies below 0.5 Hz were not plotted in the impedance and phase lag profile graphs. The mean difference in phase lag over theta was determined by subtracting the mean curves of the two groups over 3–8 Hz and calculating the mean of the curve difference.

2.6. Quantification of resonance

We measured the preferred frequency (f_{Zmax}) of each neuron as the frequency at which the impedance amplitude reached the peak, i.e., |Z_{max}| (cf. eq. 1). For simplicity, we refer throughout the text to |Z_{max}| as Z_{max}. Resonance strength was quantified using the Q value, calculated as the ratio between Z_{max} and the impedance at 0.5 Hz ($Z_{0.5\ Hz}$) (Hutcheon et al., 1996). For a more precise determination of f_{Zmax} and Q values, the experimental impedance data of every cell was fitted with a polynomial curve between 0.2 and 15 Hz to reveal Z_{max}.

2.7. Quantification of membrane capacitance

We measured the membrane capacitance in voltage clamp configuration according to the method described by Golowasch et al. (2009). In brief, neurons were held at −80 mV and a squared voltage step of −5 mV was applied for 500 ms. The capacitance was obtained as the integral of the mobilized charge divided by the voltage step.

2.8. Sample size estimation

We used the method described by Dell et al. (2002) to evaluate the sample size necessary to detect changes in the 'proportion of Res neurons' as a dichotomous variable. For an effect size of 20% (increase of Res neurons from 30 to 50%) with a power of 0.8 (1-beta) and a significance level (alpha) of 0.05, we estimated a requirement of 103 neurons per experimental group.

2.9. Monte Carlo simulation

To assess the level of confidence of the observed increase in the population of BBBd resonant neurons we measured the probability of finding a given change in the proportion of Res neurons just by chance. Monte Carlo simulations consisted on recreating our experimental samples by randomly choosing 17 neurons out of a population of 110 simulated neurons that reproduce the distribution of Res and NonRes neurons observed in control conditions (see "*Simulating a neuronal*

population…" below, and see the distribution of Q values of the population in Fig. 7B left). Next, we analyzed their resonant properties at depolarized membrane potentials to find the proportion of resonant neurons at each observation. We repeated this procedure 1000 times; obtaining independent observations that were used to generate a pseudo-empirical curve for the probability of observing a given % of Res neurons having a sampling size of 17 neurons. We display this result as a cumulative probability density (100 bins of width 1, see Fig. 2E). To have a continuous distribution we fitted a sigmoid curve, bin size 0.5.

2.10. Firing probability measurements

Firing probability under ZAP stimulation was computed for each oscillatory period as the number of sweeps in which neurons fired one or more APs divided by the total number of sweeps (typically 8). The stimulation frequency was measured as the frequency of the current stimulus at the peak of each oscillation, producing the first peak at 1.2 Hz and the last peak at 20 Hz.

2.11. Computer simulations

We simulated CA1 pyramidal neurons with a point-process conductance-based model following the Hodgkin-Huxley formalism (Hodgkin and Huxley, 1952). The model included a passive leak current (I_{Leak}), a persistent (non-inactivating) Na$^+$-current (I_{NaP}) (French et al., 1990), the slow muscarine-sensitive K$^+$-current (I_M) (Adams et al., 1982), the current of hyperpolarization-activated cyclic nucleotide-gated cation channels (I_h) (Spain et al., 1987), and the modified Hodgkin-Huxley type transient Na$^+$- and delayed-rectifier K$^+$- currents for action potential generation (I_{NaH} and I_{KH}, respectively) (Richardson et al., 2003). The equation (eq.) describing the currents flowing across the membrane is:

$$C\frac{dV}{dt} = I_{ZAP} - (I_{leak} + I_{NaP} + I_M + I_h + I_{NaH} + I_{KH}) \tag{3}$$

where C is the membrane capacitance (120 pF), V is the membrane potential in mV and I_{ZAP} is the applied current. Intrinsic ionic currents in eq. 3 followed the subsequent set of equations:

$$I_{leak} = G_{Leak}(V - E_{leak}) \tag{4}$$

$$I_{NaP} = G_{NaP}w(V - E_{Na}) \tag{5}$$

$$I_M = G_M r(V - E_K) \tag{6}$$

$$I_h = G_h(0.8f + 0.2s)(V - E_h) \tag{7}$$

$$I_{NaH} = G_{NaH}m^3h(V - E_{Na}) \tag{8}$$

$$I_{KH} = G_{KH}n^4(V - E_K) \tag{9}$$

with G_i and E_x being the time-varying conductance and reversal potential for the corresponding channel, respectively. The dynamics of the state variables $x_i = w,\ r,\ f,\ s,\ m,\ h$ and n are ruled by the following equation:

$$\frac{dx_i}{dt} = \frac{x_{i\infty}(V) - x_i}{\tau_{x_i}(V)} \tag{10}$$

where $x_{i\infty}(V)$ are the voltage-dependent steady-state values of x_i, and $\tau_{xi}(V)$ are the corresponding voltage-dependent time constants for $w,\ r,\ f$ and s. Table 1 contains the values for the conductances, the reversal potentials, the equations describing the steady-state variables, and the time constants used in the simulations. The parameters for the gating variables w and r were obtained from Vera et al. (2017), with the fast time constant for I_h increased from 38 ms to 50 ms (see Table 1) to match the f_{Zmax} of CA1 pyramidal neurons at −80 mV.

The dynamics of the state variables $m,\ h$ and n also followed eq. (10)

Table 1

Parameters and equations used for calculating ionic currents. V is the membrane potential in mV. Instantaneous process, i.e., $\tau = 0$.

Current	G_i (nS)	E (mV)	Gating variable x_∞	Time constant τ_i (ms)
I_{Leak}	15	−70	–	–
I_{NaP}	2.96–7.53	47	$w_\infty = \dfrac{1}{1 + e^{-(V+53.4)/5.22}}$	$\tau_{NaP} = 5$
I_M	7.11–62.7	−99	$r_\infty = \dfrac{1}{1 + e^{-(V+32.18)/7.35}}$	$\tau_M = \dfrac{1000}{3.3(e^{(V+35)/40} + e^{-(V+35)/20})\gamma}$
I_h	2.25	−41	$f_\infty = \dfrac{1}{1 + e^{(V+78)/7}}$ $s_\infty = \dfrac{1}{1 + e^{(V+78)/7}}$	$\tau_f = \dfrac{50}{\varphi}$ $\tau_s = \dfrac{319}{\varphi}$
I_{NaH}	1800	47	$m_\infty(V) = \dfrac{\alpha_m}{\alpha_m + \beta_m}$ $h_\infty(V) = \dfrac{\alpha_h}{\alpha_h + \beta_h}$	$\tau_m = 0$ $\tau_h = \dfrac{1}{\delta(\alpha_h + \beta_h)}$
I_{KH}	1600	−99	$n_\infty(V) = \dfrac{\alpha_n}{\alpha_n + \beta_n}$	$\tau_n = \dfrac{1}{\delta(\alpha_n + \beta_n)}$

but the voltage-dependent equilibrium values $x_{i\infty}(V)$ were calculated as:

$$x_{i\infty}(V) = \frac{\alpha_i}{\alpha_i + \beta_i} \tag{11}$$

The rate constants α_i and β_i were calculated according to a set of modified Hodgkin-Huxley equations shown in Table 2 (Richardson et al., 2003) that include modifications to adapt the model to the measured excitability of CA1 PCs: a left shift in the voltage sensitivity of α_m (from −32 mV to −55 mV), α_h (−46 mV to −52 mV), α_n (−36 mV to −38 mV), β_m (−57 mV to −65 mV), β_h (−16 mV to −22 mV) and β_n (−46 mV to −48 mV); as well as an increase in α_m slope (from 0.1 to 0.4). These changes were included in Table 2.

To simulate neurons at the same temperature at which experimental recordings were conducted (35 °C), we used temperature correction factors for modifying the time constant of I_M ($\gamma = 3^{(temp-22)/10} = 4.17$) as well as I_h ($\varphi = 4.5^{(temp-38)/10} = 0.64$) with 'temp' being the temperature in °Celsius (Magee, 1998). AP generating currents, i.e., I_{NaH} and I_{KH}, became unstable when approaching 35 °C. Therefore, I_{NaH} and I_{KH} were set to the highest temperature possible, at which the model could reproduce the firing pattern of pyramidal neurons (30 °C) by using the factor $\delta = 3^{(temp-6.3)/10} = 13.5$ (Hodgkin and Huxley, 1952). Under these conditions simulated neurons had a resting potential of ~ -65 mV and an AP threshold of ~ -51 mV when depolarized with the ZAP stimulus.

2.12. Simulating a neuronal population by using physiologically G_{NaP} and G_M values

We used a data set of published G_{NaP} and G_M values recorded in CA1 pyramidal neurons in vitro with the voltage-clamp technique (Vera et al., 2017). In brief, currents were measured by the subtraction method after blocking each current with a selective drug (TTX for I_{NaP}, XE991 for I_M). The subtracted current trace was transformed to a conductance over voltage trace ($g_{i\infty}(V)$), and the maximal conductance (G_i) was computed by fitting the theoretical function:

$$g_{i\infty}(V) = G_i \frac{1}{1 + e^{\frac{V - V_i}{s_i}}} \tag{12}$$

where G_i is the maximal conductance in nS, V the membrane potential in

Table 2

Equations used for calculations of rate constant α_x and β_x. V is the membrane potential in mV.

	α_x	β_x
m	$\dfrac{-0.1(V+55)}{e^{-0.4(V+55)} - 1}$	$4e^{-(V+65)/18}$
h	$0.07e^{-(V+52)/20}$	$\dfrac{1}{e^{-0.1(V+22)} + 1}$
n	$\dfrac{-0.1(V+38)}{e^{-0.1(V+38)} - 1}$	$0.125e^{-(V+48)/80}$

mV, V_i the voltage at half activation, and s_i the slope of the curve. We used a data set containing the G_{NaP} values from 11 neurons (in nS: 2.96, 3.92, 4.79, 4.88, 5.16, 5.84, 5.87, 6.04, 6.8, 7.45 and 7.53; mean ± SD: 5.57 ± 1.41), and G_M values from 10 neurons (in nS: 3.95, 4.50, 4.96, 6.06, 6.90, 7.33, 7.49, 19.52, 24.10, 34.81; mean ± SD: 11.96 ± 10.52) from dorsal hippocampus. Out of these 10 G_{NaP} and 11 G_M conductances we used the possible 110 combinatorial sets to simulate 110 distinct neurons. We noticed that when using those G_M values, we obtained an average Q value of ~1.2 at depolarized subthreshold potential, reproducing well the Q values obtained from PCs in young rats (Vera et al., 2017). To reproduce the Q values, we obtained from PCs of adult sham rats, it was necessary to increase the resonant generating conductance G_M by a factor of 1.8 (80% increase in each value), achieving a Q value of ~1.7. Neuronal responses were simulated using a time resolution of 10 μs.

2.13. Sensitivity analysis of simulated CA1 pyramidal neurons and simulations of BBBd condition

We evaluated the contribution of I_{Leak}, I_{NaP} and I_M to subthreshold excitability of CA1 pyramidal neurons by increasing I_{Leak} or I_M, or by decreasing I_{NaP} in 20% steps the maximal conductance of each current. For each step all 110 modeled neurons were simulated under ZAP stimulation at subthreshold (1 pA below reaching the AP threshold) and suprathreshold potentials (minimal potential for evoking APs under ZAP stimulation).

To simulate the BBBd conditions we explored different increases of G_M in all neurons to reproduce the proportional increase in Res and the concomitant decrease in NonRes neurons. To also reproduce the changes in intrinsic properties in NonRes neurons in BBBd, we either reduced G_{NaP} or increased G_{Leak} in only those neurons that kept being NonRes after the increase in G_M. We find that the two conditions that best reproduced our experimental observations were a 50% increase in G_M in all neurons plus a 20% reduction in G_{NaP} in NonRes neurons (MBBBd1) or a 60% increase in G_M in all neurons plus a 23% increase in G_{Leak} in NonRes neurons (MBBBd2).

2.14. Simulation analysis and code accessibility

Simulated voltage responses were analyzed using the same software and codes used for the experimental data. Simulations and analysis were performed with Igor Pro 7.0 software (WaveMetrics, Inc., OR, USA) using custom scripts, all of which are available in GitHub (https://github.com/jorgeverab/HipocampalEpileptogenesis).

2.15. Statistical analysis

For statistical analysis, data from sham and BBBd groups were first tested for Gaussian distribution using the Shapiro-Wilk test. Normally distributed data were presented as mean ± standard error of the mean (SEM) and tested for statistical significance using the Student's t-test.

Not-normally distributed data were presented as the median and its upper (Q3) and lower quartile (Q1). For non-parametric statistics the Mann–Whitney-U (MW) test was used and categorical data was compared using the Chi-square test (Graph Pad Software, CA, USA). Data were presented as statistically significant when the *p* value was smaller than 0.05. Data were tested using the Igor Pro software.

3. Results

3.1. Hippocampal theta resonance in a model of post-stroke epileptogenesis

We evaluated the impact of cortical photothrombosis on intrinsic frequency preference in hippocampal pyramidal cells using the established photothrombotic stroke model (Watson et al., 1984). To induce a cortical photothrombosis we intravenously injected the photosensitizer Rose bengal (20 mg/kg bodyweight) and exposed the right hemisphere through the intact skull with intense light (light guide $\varnothing$ = 3.5 mm, 150 W halogen lamp) for 15 min (Fig. 1A, upper panel). Within a few minutes cortical brain vessels clot (Schoknecht et al., 2014) producing a cortical photothrombosis (Fig. 1A, B: upper panel) and in the subsequent hours a blood-brain barrier dysfunction develops in the subjacent dorsal hippocampus as shown previously in several of our studies (Kim et al., 2017; Lapilover et al., 2012; Lippmann et al., 2017). After one week the BBBd- and sham-operated animals were sacrificed, and acute hippocampal slices for patch-clamp recordings from PCs were prepared (Fig. 1B). In the current-clamp configuration, sinusoidal ZAP stimuli were applied, followed by a hyperpolarizing current step (Fig. 1C, upper panel). From the corresponding membrane potential (V_m) the impedance curve and the input resistance (R_{in}) of the cell were calculated. The resonance strength (Q value = $Z_{max}/Z_{0.5\ Hz}$) (Koch, 1984), was determined from each cell at depolarized subthreshold V_m. Q values show a bimodal distribution with Res neurons displaying values higher than 1.1 while NonRes neurons have values centered at 1.0 (Vera et al., 2014, 2017, and see Figs. 2C and 7B left). Therefore, we grouped cells according to their Q values as 'resonant' (Res, Q > 1.1) or 'non-resonant' (NonRes, Q ≤ 1.1). Res neurons display their resonance frequency at maximal impedance (f_{Zmax}) predominantly within the theta range (3–8 Hz), while the f_{Zmax} of NonRes neurons occurs at lower frequencies

(Fig. 1C, lower panel).

3.2. Post-stroke epileptogenesis increases the percentage of hippocampal theta resonant neurons

Since we previously observed increased hippocampal theta network activity during post-stroke epileptogenesis (as detected by in vivo field potential recordings, Lippmann et al., 2017), we first asked whether this change in network activity could be related to increased resonance properties of individual neurons and/or due to an increased proportion of neurons expressing resonance behavior. To address this question, we used a stimulation protocol aiming to evaluate whether PCs 'prefer' theta oscillations and fire APs selectively at theta frequencies (Vera et al., 2017). We performed whole-cell current-clamp recordings and applied ZAP current stimuli at two nearby but different perithreshold (i. e., around the AP threshold) potentials. We explored the 'depolarized subthreshold V_m' (subsequently abbreviated as 'subthreshold V_m') by depolarizing neurons just below the AP threshold when applying the ZAP stimulus, and the 'suprathreshold V_m' by depolarizing neurons so they start firing at least one AP per sweep of the ZAP stimulus (Fig. 2A). Therewith, we could evaluate whether PCs express theta resonance before firing APs and whether PCs are effective in firing APs at theta frequencies to communicate this rhythm to downstream neurons. Because perithreshold theta resonance and AP firing at theta frequency are most likely to impact theta network activity, we focused our analysis on the perithreshold voltage range (see below).

Fig. 2A presents exemplary voltage responses of a sham non-resonant (grey) and a sham resonant neuron (black) at perithreshold potentials. The black traces show the resonant voltage responses in the theta range, which is the hallmark of Res neurons, and the typical occurrence of spikes at higher frequencies in the Res neuron compared to the NonRes neuron. The averaged impedance profile for sham resonant neurons showed that at subthreshold V_m their Z_{max} was located in the theta frequency range (Fig. 2B), while the Z_{max} of non-resonant neurons was located at a lower frequency. When analyzing the Q values for sham and BBBd neurons, we found in each group two distinct neuronal populations. One population peaked at Q = 1 comprising NonRes neurons and a second distinct population dispersed above Q = 1.1 matching the Res neurons (Fig. 2C, Table 3). Previously, we have shown that 24% of
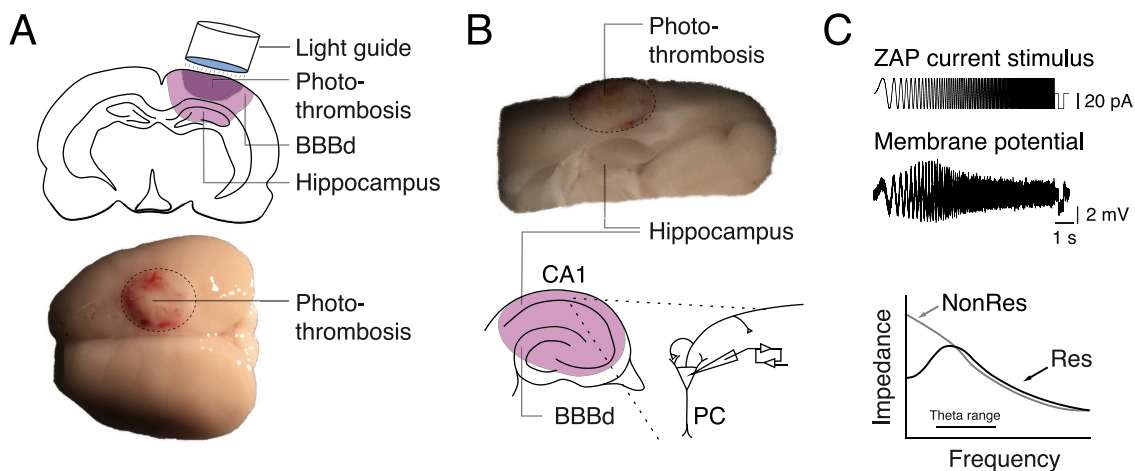

Fig. 1. Experimental design for studying theta resonance in hippocampal neurons after a cortical photothrombosis. **A.** Upper panel: Blood-brain barrier-dysfunction (BBBd, light magenta) is induced by cortical photothrombosis (dark magenta), i.e., by a light-dependent activation of the intravenously applied photosensitizer Rose bengal. BBBd occurs within one day and typically leads to post-stroke epileptogenesis within one week (see methods for details). Lower panel: Photograph of a brain with a cortical photothrombosis. **B.** Upper panel: Parasagittal slice showing the hippocampus right underneath the cortical photothrombosis. Lower panel: Membrane potential changes are recorded from pyramidal cells (PC) in hippocampal area CA1 in the current-clamp configuration. Light magenta area indicates the area most affected by BBBd, as previously shown (Kim et al., 2017; Lapilover et al., 2012; Lippmann et al., 2017). **C.** Upper panel: ZAP ('impedance amplitude profile') current stimulus and corresponding changes in the membrane potential. The example shows a characteristic theta-range resonant voltage response. Lower panel: Scheme of typical impedances plotted vs. frequency. The two schematic example traces are from neurons with resonant (Res) and non-resonant (NonRes) voltage responses in the theta range. (For interpretation of the references to colour in this figure legend, the reader is referred to the web version of this article.)
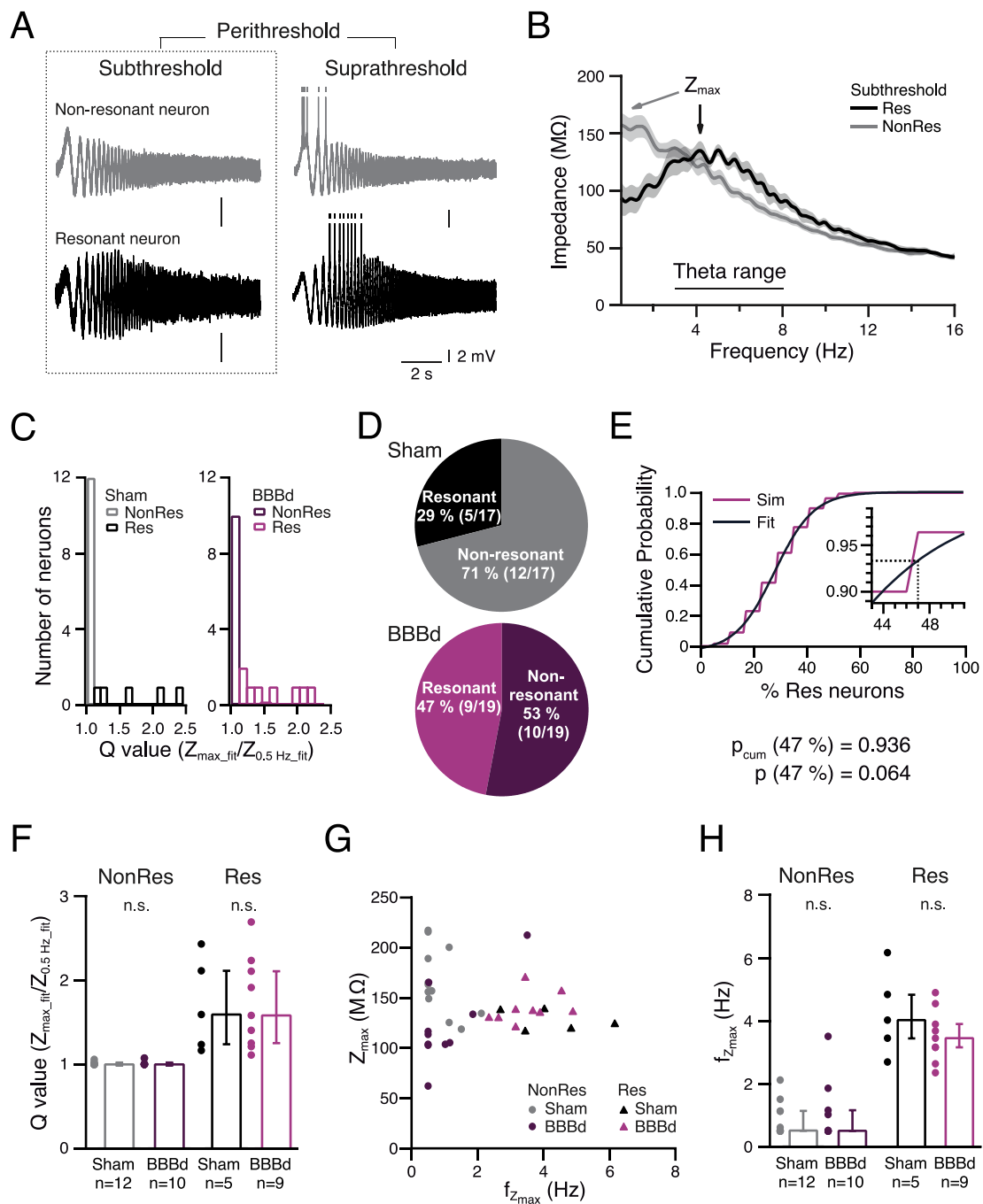
Fig. 2. Increased fraction of hippocampal neurons displaying perithreshold theta-resonance in post-stroke epileptogenesis. **A.** Example voltage responses of a sham non-resonant (grey) and resonant neuron (black) in response to ZAP current stimuli at different perithreshold membrane potentials (V_m; subthreshold: -65.0 mV (NonRes), -58.5 mV (Res); suprathreshold: -64.0 mV (NonRes), -57.0 mV (Res); all vertical scale bars: 2 mV). **B.** Average impedance plotted vs. frequency of sham Res ($n = 5$) and NonRes neurons ($n = 12$) at subthreshold V_m. Arrows point at the maximal impedances (Z_{max}). Shaded areas indicate the SEM of the curves. **C.** Histograms of number of neurons containing Q values [Z_{max} over impedance at 0.5 Hz ($Z_{0.5Hz}$) of fitted data to smooth scattering] of sham (left panel) and BBBd (right panel) treatment groups. Colour codes reveal assignment to distinct neuronal groups. **D.** Proportion of resonant and non-resonant neurons at perithreshold potential for neurons from sham and BBBd treated animals (Chi-square test $p = 0.27$). **E.** Cumulative probability density curve displaying the probability of observing a given proportion of Res neurons with a sample size of 17 neurons using Monte Carlo simulations. Inset, zoom in at 47% Res neurons. **F.** Subthreshold resonance strength (Q value) of NonRes and Res neurons from sham- and BBBd-treated animals. **G.** Subthreshold Z_{max} plotted vs. frequency at maximal impedance (f_{Zmax}) for all recorded neurons. **H.** Quantification of subthreshold f_{Zmax} between NonRes and Res neurons.

PCs display perithreshold theta resonance in young naïve rats, while the remaining 76% of neurons do not show perithreshold resonance because the combination of I_M and I_{NaP} would cause neurons to resonate above the action potential threshold and neurons would not be capable of firing with theta preference (Vera et al., 2017). For sham-treated adult rats we found a similar percentage of 29% Res neurons (5 out of 17 cells). In contrast, the percentage of resonant neurons in BBBd-treated rats was 47% (9 out of 19 cells), representing a relative increase of 62% in the proportion of resonant neurons (Fig. 2D, Chi-square test $p = 0.27$). As finding statistical significance based on theoretical distributions requires a high sample size (we calculated more than 100 neurons per experimental group, see Methods "Sample size estimation"), we

Table 3

Intrinsic electrophysiologically properties obtained from sham and BBBd resonant (Res) as well as non-resonant neurons (NonRes). Values were obtained at hyperpolarized (Hyper), near resting (Rest), subthreshold (Sub) and suprathreshold (Supra) membrane potentials (V_m). n - number of neurons, R_{in} – input resistance, Z_{max} – maximal impedance, Q value – resonance strength, f_{Zmax} – frequency at maximum impedance, Φ_{6Hz} – phase lag at 6 Hz, Φ_{fZmax} – phase lag at f_{Zmax}. For simplicity all values given as mean ± SEM, *indicates statistical significance. Not normally distributed values, statistical tests and p values are described in the main text. Note that neurons were assigned to the Res or NonRes group according to their frequency response at subthreshold V_m.

Res		n	V_m(mV)	R_{in}(MΩ)	Z_{max}(MΩ)	Q value	f_{Zmax}(Hz)	Φ_{6Hz}(°)	Φ_{fZmax}(°)
Hyper	Sham	5	-79.0 ± 0.5	49.5 ± 3.5	57.5 ± 2.0	1.13 ± 0.02	4.4 ± 0.20	-24.5 ± 2.0	-14.5 ± 2.0
	BBBd	9	-79.5 ± 0.0	51.0 ± 2.0	58.0 ± 2.5	1.15 ± 0.02	4.4 ± 0.30	-25.0 ± 1.5	-16.0 ± 1.0
Rest	Sham	5	-67.5 ± 0.5	69.5 ± 11.5	83.0 ± 3.5	1.09 ± 0.05	2.2 ± 0.50	-37.5 ± 0.5	-11.0 ± 2.0
	BBBd	9	-68.0 ± 0.5	75.5 ± 4.5	81.0 ± 4.0	1.06 ± 0.02	2.1 ± 0.35	-38.5 ± 1.5	-12.0 ± 1.0
Sub	Sham	5	-58.0 ± 1.0	90.0 ± 10.0	127.0 ± 4.5	1.71 ± 0.25	4.3 ± 0.60	-36.5 ± 5.5	-19.0 ± 2.0
	BBBd	9	-60.5 ± 0.5*	94.0 ± 5.0	139.0 ± 5.0	1.72 ± 0.18	3.6 ± 0.30	-50.0 ± 3.0*	-18.0 ± 2.0
Supra	Sham	5	-57.0 ± 1.0	78.5 ± 8.5	125.5 ± 11.0	1.61 ± 0.11	4.7 ± 0.50	-34.5 ± 8.0	-18.0 ± 3.5
	BBBd	9	-60.0 ± 0.5*	86.0 ± 6.0	137.0 ± 5.5	1.71 ± 0.16	4.3 ± 0.25	-46.5 ± 4.0	-20.0 ± 2.5
NonRes		**n**	V_m(mV)	R_{in}(MΩ)	Z_{max}(MΩ)	Q value	f_{Zmax}(Hz)	Φ_{6Hz}(°)	Φ_{fZmax}(°)
Hyper	Sham	12	-78.5 ± 0.0	61.0 ± 3.0	71.5 ± 2.5	1.11 ± 0.00	4.0 ± 0.40	-27.5 ± 1.5	-15.0 ± 0.5
	BBBd	10	-78.5 ± 0.5	55.0 ± 4.0	58.0 ± 4.5*	1.12 ± 0.00	4.4 ± 0.40	-24.0 ± 2.5	-13.0 ± 1.0
Rest	Sham	11	-68.5 ± 0.5	85.0 ± 5.0	100.5 ± 7.0	1.04 ± 0.01	1.7 ± 0.30	-39.0 ± 1.5	-11.0 ± 1.0
	BBBd	10	-68.5 ± 0.5	71.5 ± 6.5	79.0 ± 8.0	1.06 ± 0.03	1.7 ± 0.40	-33.5 ± 3.0	-8.0 ± 2.5
Sub	Sham	12	-63.0 ± 0.5	130.5 ± 8.0	166.0 ± 9.5	1.01 ± 0.01	0.9 ± 0.15	-50.5 ± 2.0	-10.5 ± 2.5
	BBBd	10	-60.5 ± 1.5	100.5 ± 10.0*	122.0 ± 13.0*	1.02 ± 0.01	1.1 ± 0.30	-45.0 ± 2.0	-10.0 ± 2.0
Supra	Sham	12	-60.5 ± 0.5	142.5 ± 5.0	184.0 ± 9.5	1.09 ± 0.03	1.9 ± 0.40	-55.0 ± 1.5	-16.0 ± 3.5
	BBBd	9	-57.0 ± 1.5*	114.5 ± 12.0*	148.0 ± 15.0*	1.21 ± 0.10	2.2 ± 0.65	-50.0 ± 3.5	-13.0 ± 4.5

opted for a more empirical approach. We simulated a heterogeneous population of PCs ($n = 110$) that reproduced remarkable well the distribution of Q values of naïve and sham PCs (including resonant properties and intrinsic parameters, see Methods). By using Monte Carlo simulations, we randomly chose 17 neurons out of the simulated population, analyzed their resonant properties and computed the proportion of Res neurons for 1000 independent times. This allowed us to build a pseudo-empirical curve of probability for finding a given proportion of Res neurons constrained by our sampling size (see Methods). The curve at Fig. 2E summarizes the result of the simulations as a cumulative probability density for the percentage of Res neurons, and shows that the most probable outcome is to obtain 30% of Res neurons ($p_{cum} = 0.5$). This value is in agreement with our previous report (Vera et al., 2017) and with our percentage in the sham condition. Interestingly, the probability of obtaining 47% of Res neurons (BBBd) by chance is as low as 0.064 ($p_{cum} = 0.936$) (Fig. 2E). While we are aware that our confidence is little above the standard of $p = 0.05$, we consider i) the consistent finding of ~30% of Res neurons across independent experimental groups, different laboratories and computer simulations, as well as ii) the fact that BBBd and sham animals were processed under the same conditions, as highly supportive that our finding reveal an increase in the proportion of Res neurons caused by the post-stroke epileptogenesis. Interestingly, despite this difference in the proportion of cell numbers, both BBBd and sham neurons display similar resonance strength (Q values) within the Res and NonRes groups (Fig. 2F, for values see Table 3). Plotting Z_{max} against the resonance frequency at maximal impedance (f_{Zmax}) reveals similar ranges for f_{Zmax} in NonRes and Res neurons between sham and BBBd (Fig. 2G-H, Table 3), while potential differences can be assumed for Z_{max} in NonRes neurons (see Fig. 5C). We also measured resonant properties at hyperpolarized (I_h-dependent) and resting membrane potentials (no resonance) by changing the holding current and directing cells to −80 mV or resting V_m ($I = 0$), respectively. However, we neither found major changes between treatment groups at hyperpolarized (except Z_{max} in NonRes) nor at resting V_m (Table 3), supporting our hypothesis that perithreshold theta resonance may be more affected and may underlie an increased theta resonance.

These results show that rats undergoing post-stroke epileptogenesis exhibit similar resonance properties (Q and f_{Zmax}) at all membrane potentials in the hippocampus but that the percentage of neurons expressing perithreshold resonance behavior is increased in BBBd. As a larger number of resonant cells at depolarized potential might contribute with a stronger firing at theta range, this result is in agreement with the observation of an enhanced theta network activity in vivo (Lippmann et al., 2017).

3.3. Resonant neurons preserve intrinsic properties at subthreshold potentials in epileptogenesis

We investigated further intrinsic properties at perithreshold potentials. As particularly the frequency-dependent impedance differs between Res and NonRes neurons (Fig. 2B), we measured the peak impedance (Z_{max}), input resistance (R_{in}), and phase-lag (Φ) at different membrane potentials (Fig. 3 and Table 3). At subsubthreshold potential representative voltage responses displayed similar bandpass filtering in both conditions (Fig. 3A), resulting in similar resonance strength in the theta range in BBBd and sham resonant neurons (Fig. 3A, Table 3). Analogous, the averaged impedance profiles (Fig. 3B) and peak impedances revealed similar values (Fig. 3C, t-test $p = 0.11$). Similarly, the input resistance (R_{in}) showed comparable values in BBBd and sham neurons (Fig. 3D and Table 3, t-test $p = 0.36$). When comparing the phase lags, i.e., the delay between the current stimulus and the voltage response (Fig. 3E), BBBd resonant neurons displayed slightly larger phase-lag values over all tested frequencies (Fig. 3F) and a mean increase of 8.9° over the theta frequency range (3–8 Hz). To quantify this shift at a frequency relevant for theta oscillations, we measured the
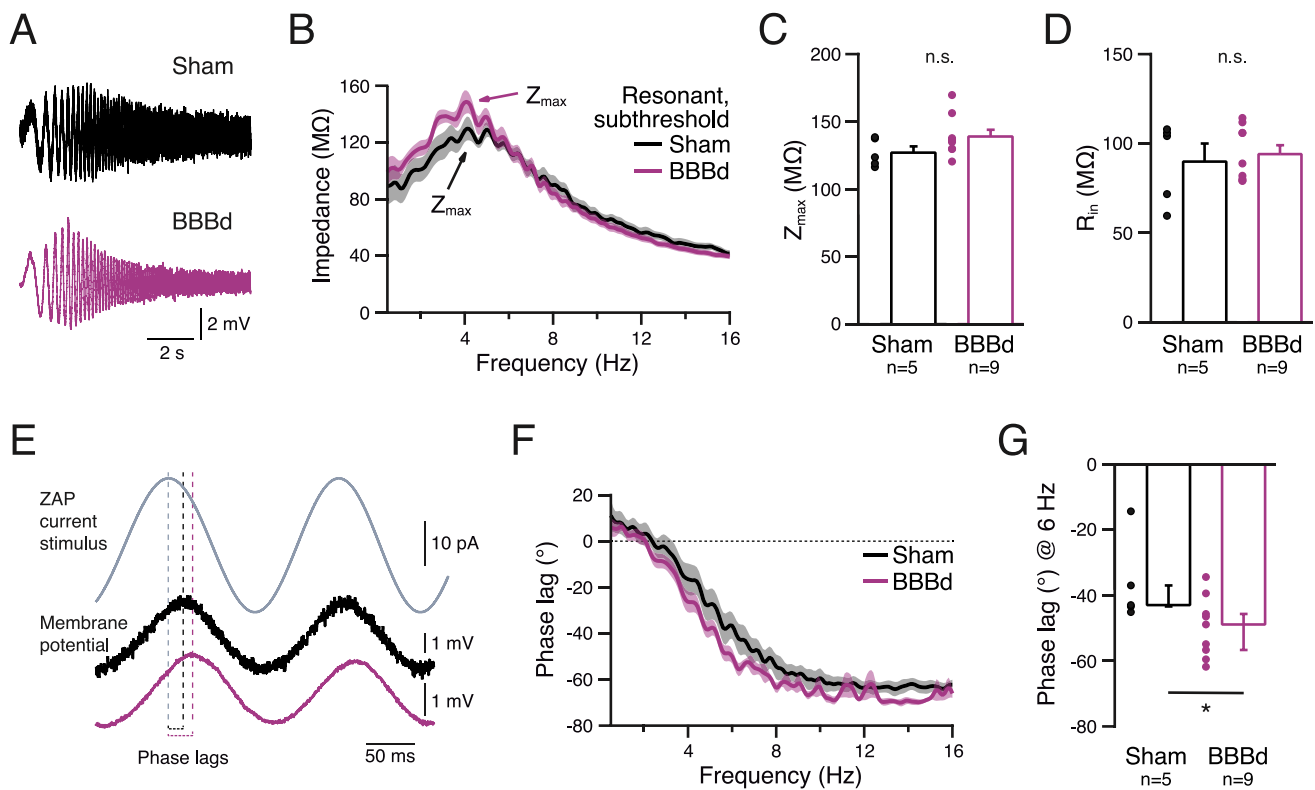
Fig. 3. After undergoing BBBd, resonant neurons show an increased phase lag at subthreshold membrane potential. **A.** Exemplary voltage responses to ZAP current stimuli from a typical sham (top) and BBBd resonant neuron (bottom). **B.** Averaged impedances (mean ± SEM) plotted vs. frequency, where the Z_{max} values were determined from a polynomial fit to the data (not shown). **C-D.** Maximal impedance and input resistance of sham and BBBd resonant neurons (individual data points and mean + SEM). **E.** ZAP current stimulus (blue-grey) with corresponding exemplary voltage responses from a sham (black) and BBBd resonant neuron (magenta), illustrating the different phase lags between current input and voltage responses. **F.** Averaged phase lags (mean ± SEM) plotted over the full frequency range of the ZAP stimulus. **G.** Quantification of phase lags of sham and BBBd resonant neurons at the representative theta frequency of 6 Hz (median + Q3/−Q1, Mann-Whitney U test (MW) $p = 0.042$). (For interpretation of the references to colour in this figure legend, the reader is referred to the web version of this article.)

phase-lag at 6 Hz (Φ_{6Hz}), finding an increase of 6° in BBBd neurons (Fig. 3G, median Q3/Q1, sham: −43.0 6.0/0.5° and BBBd: −49.0 3.0/8.0°, MW $p = 0.042$). This corresponds to a shift of ~3 ms at 6 Hz. As changes in dendritic morphology have been associated with epilepsy (Casanova et al., 2014; Mattson et al., 1989; Swann et al., 2000), we also measured the membrane capacitance as an approximation to explore modifications of the cell morphology. We find that Res neurons display similar capacitance values (sham: 163.0 ± 12.0 pF and BBBd: 162.5 ± 7.5 pF, t-test $p = 0.96$), suggesting that the hippocampal BBBd did not produce major changes in cell morphology.

3.4. Hippocampal resonant neurons are more excitable in post-stroke epileptogenesis

We next analyzed the excitability of resonant neurons during epileptogenesis by applying ZAP stimuli at suprathreshold potentials, i.e., the potential at which the given neuron started firing APs. (Fig. 4A, B). Both sham and BBBd neurons generated APs with higher probabilities in the 2–6 Hz range, while firing at frequencies below 2 Hz was almost absent (data for example traces: Fig. 4D-E). Resonant neurons of both groups reacted equally, both by firing a similar number of total APs (Fig. 4C, sham: 12.0 ± 2.5 vs. BBBd: 11.0 ± 2.1, t-test $p = 0.77$) and by expressing a similar firing probability in the theta range, thus confirming the interaction of their resonant behavior with the generation of APs (Fig. 4F). Because not only the number and frequency of spikes are important but also the excitability parameters like resting V_m and the membrane potential at which neurons started firing, we next analyzed whether these parameters were altered in Res neurons of potentially epileptogenic rats. Although the resting V_m was similar in sham and

BBBd neurons (Fig. 4G, median Q3/Q1, sham: −72.0 1.0/6.0 mV vs. BBBd: −75.5 1.5/0.5 mV, MW $p = 0.86$), the suprathreshold V_m (measured as the average of the voltage trace during the ZAP response) shifted 4 mV towards more hyperpolarized potentials in BBBd neurons (Fig. 4H, median Q3/Q1 sham: −56.5 1.5/2.0 mV vs. BBBd: −60.5 1.0/0.5 mV, MW $p = 0.042$). One possible cause underlying this observation could be a lowered AP threshold (the V_m at which dV/dt exceeds 5 mV/ms). Indeed, the AP threshold was more hyperpolarized by 6 mV, although not quite reaching statistical significance (Fig. 4I, median Q3/Q1 sham: −52.0 1.5/2.0 mV vs. BBBd: −46.0 5.0/0.0 mV, MW $p = 0.060$). To investigate the membrane potential at which I_M and I_{NaP} most intensively interact to generate theta resonance, we further measured the perithreshold V_m, i.e., the V_m 30 ms before the AP threshold (average of 10 ms window). In fact, BBBd Res neurons reached their perithreshold V_m at a significantly lower potential than sham Res neurons (Fig. 4J, median Q3/Q1 sham: −49.5 4.5/0.0 mV vs. BBBd: −55.0 1.0/2.0 mV, MW p = 0.042). Although the AP threshold did not quite reach statistical significance (p = 0.06), probably due to the small number of neurons, these results show that resonant neurons from BBBd rats require less depolarization to reach the supra- and perithreshold potentials, a strong sign of being more excitable and susceptible for generating theta resonance. Taken together, BBBd treated rats display a larger percentage of resonant neurons that are also more excitable.

3.5. In post-stroke epileptogenesis hippocampal non-resonant neurons show reduced subthreshold impedance

As performed for resonant neurons (Fig. 3), we next quantified the intrinsic properties of non-resonant neurons (Fig. 5). Fig. 5A-B show
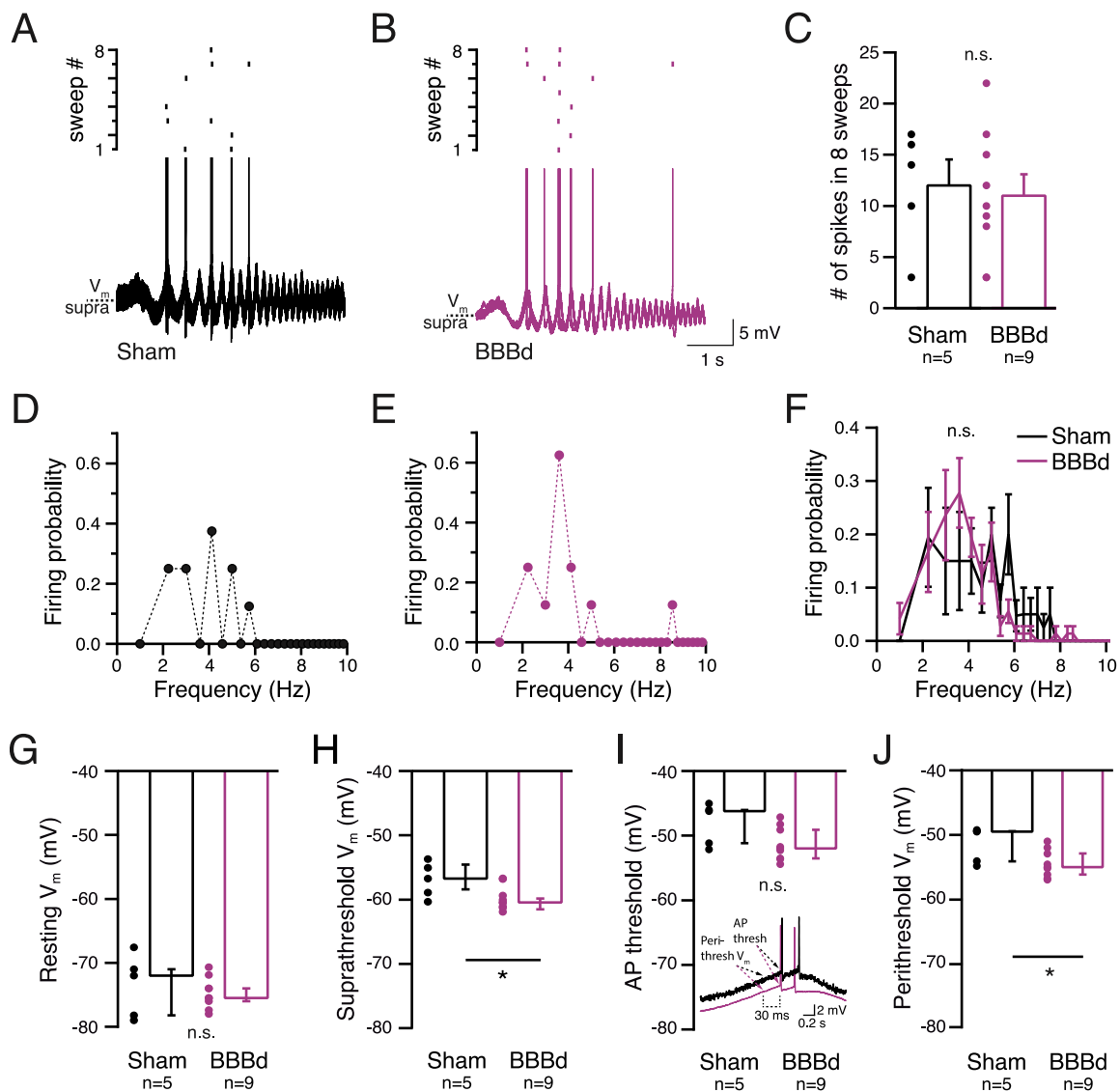
Fig. 4. In post-stroke epileptogenesis, hippocampal resonant neurons fire at more hyperpolarized potentials. **A-B.** Overlaid suprathreshold voltage responses (bottom) from eight consecutive sweeps with marks of the corresponding APs per sweep (top) from a sham (A) and a BBBd resonant neuron (B). Dotted line represents the suprathreshold V_m. **C.** Total number of spikes out of eight sweeps in sham and BBBd Res neurons. **D-E.** Firing probability over frequency per eight sweeps from the examples shown in A-B. **F.** Averaged firing probability of sham and BBBd resonant neurons (mean ± SEM). **G-H.** Resting V_m and suprathreshold V_m (MW p = 0.042) of sham and BBBd resonant neurons. **I-J.** Traces in I display exemplary zoom ins of suprathreshold voltage responses depicting the AP threshold and the perithreshold V_m (30 ms before the AP threshold) for sham (black) and BBBd (magenta). Comparison of AP threshold (MW p = 0.060) and perithreshold V_m (MW p = 0.042) for sham and BBBd Res neurons. (For interpretation of the references to colour in this figure legend, the reader is referred to the web version of this article.)

representative voltage traces and averaged impedance profiles for BBBd and sham non-resonant neurons at subthreshold potential. The voltage traces show the typical maximal response at frequencies close to 0 Hz, which was substantially reduced in the BBBd example neuron. Also, on average (Fig. 5C) the peak impedance was strongly reduced in BBBd neurons (sham: 166.0 ± 9.5 MΩ and BBBd: 122.0 ± 13.0 MΩ, t-test p = 0.014). Similarly, R_{in} was significantly diminished in BBBd neurons (Fig. 5D, sham: 130.5 ± 8.0 MΩ and BBBd: 100.5 ± 10.0 MΩ, t-test p = 0.027). The reduction of peak impedance and R_{in} can be associated with an increase in the total membrane conductance (more open channels) and/or with an increase in the total cellular membrane surface due to an enlargement of the dendritic tree. Both groups of neurons show similar membrane capacitances (median Q3/Q1 sham: 145.5 10.0/9.0 pF vs. BBBd: 156.0 50.0/9.0 pF, MW p = 0.16), supporting the former possibility. In contrast to Res neurons, no significant shift in phase-lag occurred in BBBd NonRes neurons (Fig. 5E-F), particularly not in the theta range (Fig. 5F-G, mean difference over 3–8 Hz: 6.1°, @ 6 Hz sham:

−50.5 ± 2.0° vs. BBBd: −45.0 ± 2.0°, t-test p = 0.08). Thus, NonRes neurons (Fig. 5) show changes in intrinsic properties (Z_{max}, R_{in}, and presumably phase-lag) that are contrasting those occurring in Res neurons (Fig. 3; change in phase-lag but neither in Z_{max} nor in R_{in}).

3.6. Hippocampal non-resonant neurons are less excitable in post-stroke epileptogenesis

As for resonant neurons (Fig. 4), we analyzed the excitability of non-resonant neurons during epileptogenesis (Fig. 6). Similarly, we first explored the firing probability at suprathreshold potentials (Fig. 6A-B) and found, as expected, that sham NonRes neurons fired preferentially at frequencies below 3 Hz, whereas BBBd NonRes neurons showed a reduced frequency preference (representative examples in Fig. 6D-E); the total number of spikes was not significantly different in the two groups (Fig. 6C, median Q3/Q1, sham: 24 7/12 vs. BBBd: 8 15/6, MW p = 0.1), confirming that both cell groups were depolarized to equivalent
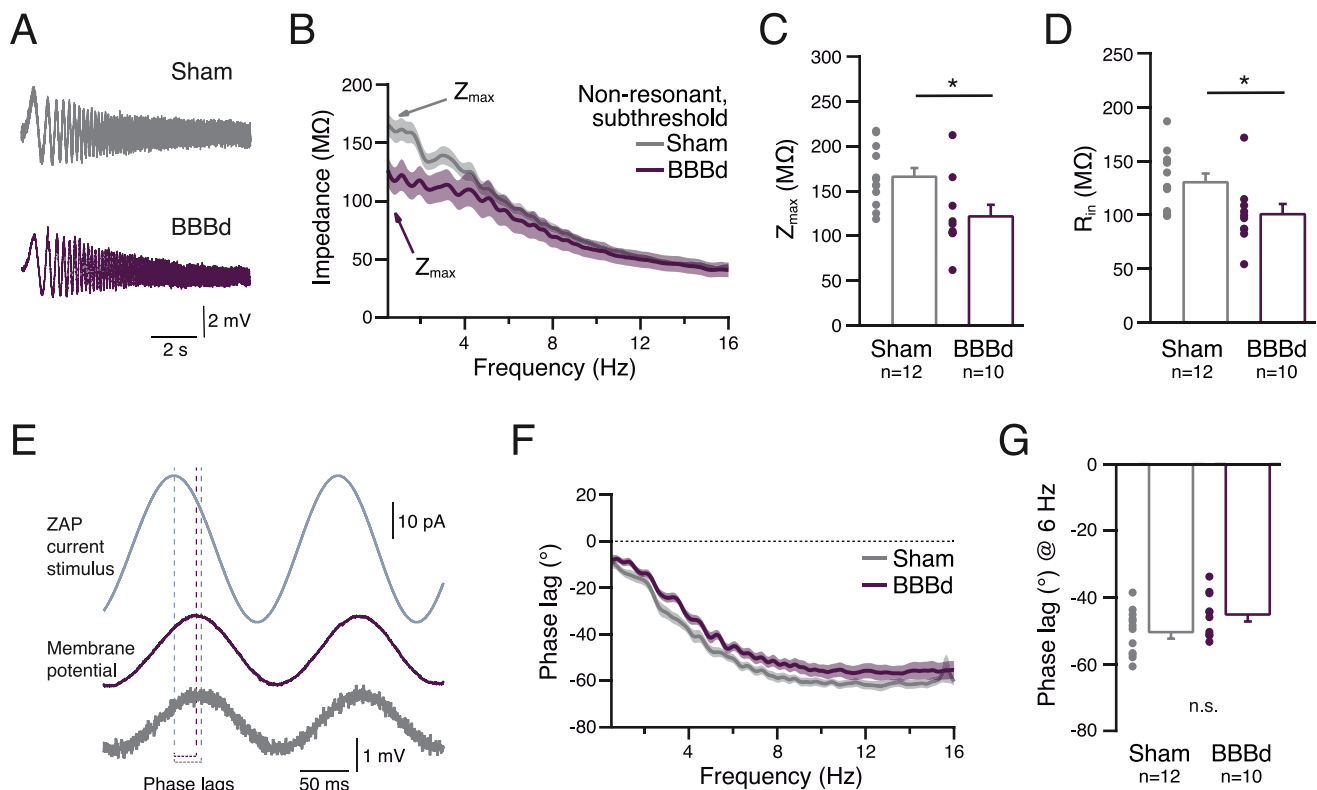
Fig. 5. In post-stroke epileptogenesis, hippocampal non-resonant neurons show decreased impedance and input resistance at subthreshold membrane potentials. Same analysis as in Fig. 3 but for non-resonant neurons. **A.** Exemplary voltage responses to ZAP current stimuli from a typical sham (top) and BBBd non-resonant neuron (bottom). **B.** Averaged impedance vs. frequency plots. **C-D.** Maximal impedance and input resistance of sham and BBBd non-resonant neurons (Z_{max}: *t*-test p = 0.014, R_{in}: t-test p = 0.027). **E.** Phase lag examples from a sham (grey) and a BBBd non-resonant neuron (purple). **F.** Averaged phase lags plotted over the full frequency range of the ZAP stimulus. **G.** Phase lags of sham and BBBd non-resonant neurons at 6 Hz. (For interpretation of the references to colour in this figure legend, the reader is referred to the web version of this article.)

levels relative to the AP threshold. Notably, sham NonRes neurons revealed an average firing probability close to 1 for the lowest explored frequency (~1 Hz), whereas the firing probability of BBBd NonRes neurons was significantly reduced to ~0.4 in that range (Fig. 6F, at 1 Hz: sham 0.75 ± 0.1 vs. BBBd 0.39 ± 0.1, MW p = 0.03). This suggests that BBBd NonRes neurons may express some sort of a low-pass filter, reducing the amplitude of oscillations close to 0 Hz, and therefore expressing some resemblance to Res neurons.

As in Res neurons (Fig. 4), the resting V_m was similar between groups (Fig. 6G, median Q3/Q1, sham: −74.0 2.5/1.5 vs. BBBd: 74.5 1.5/3.0, MW p = 0.78). However, the suprathreshold V_m (Fig. 6H, sham: −60.5 ± 0.5 vs. BBBd −57.0 ± 1.5, t-test p = 0.041) was significantly more positive in BBBd compared to sham NonRes neurons. Furthermore, the AP threshold (Fig. 6I, sham: median Q3/Q1 sham: −51.5 2.5/1.5 mV vs. BBBd: −49.0 1.0/3.5 mV, MW p = 0.012) as well as the perithreshold V_m (Fig. 6J, sham: −54.5 ± 0.5 vs. BBBd −50.5 ± 1.5, t-test p = 0.036) revealed significantly more positive values in BBBd neurons. Having more depolarized suprathreshold V_m, AP threshold as well as peri-threshold V_m imply that NonRes BBBd neurons require more excitatory inputs to start firing. Therefore, NonRes neurons are less excitable in two ways, first by having a reduced R_{in} and second by displaying a more depolarized AP threshold (Figure 5 and 6). These findings contrast those from Res neurons, which showed significantly more negative potentials (cf. Fig. 4H, J). Taken together, BBBd NonRes neurons displayed a reduced preference for firing at below-theta frequencies and show, in opposite to BBBd Res neurons, more depolarized AP thresholds, both factors producing a reduction in their excitability.

3.7. Modulation of subthreshold intrinsic conductances can account for changes observed in post-stroke epileptogenesis

Since we observed that post-stroke epileptogenesis is associated with altered intrinsic properties of hippocampal pyramidal neurons, we aimed at identifying candidate conductances that could underlie the observed increase in the proportion of resonant neurons as well as the observed changes in excitability of both Res and NonRes neurons. For this purpose, we developed a comprehensive conductance-based computational model of CA1 pyramidal neurons using the Hodgkin and Huxley formalism. To reproduce the heterogeneity of intrinsic properties observed in our sham experiments (see Methods) we used the same population of simulated neurons used in the Monte Carlo simulations. This population consisted of 110 simulated neurons using a published set of conductances for I_{NaP} and I_M that were measured under voltage-clamp experiments in CA1 neurons (Vera et al., 2017) (see Methods). To validate our simulated population of PCs, we first investigated whether simulated neurons were able to display the variety of resonant and non-resonant behaviors observed experimentally. To this end we simulated the ZAP protocol at subthreshold potential in the same way we conducted the experiments (with a holding current 1 pA below the current necessary to induce AP firing). Fig. 7A displays representative traces from a simulated Res and NonRes neuron at sub- and suprathreshold potentials. Res neurons bandpass filter inputs and fire at theta frequencies, while NonRes neurons amplify lower frequency inputs and fire at the lowest tested frequencies, identical to hippocampal neurons in sham condition. When analyzing the resonant properties of simulated neurons, we find that the Q values of the simulated population show a bimodal distribution, with one component that peaks at Q = 1 containing NonRes neurons (70%, mean ± SEM: 1.01 ± 0.015
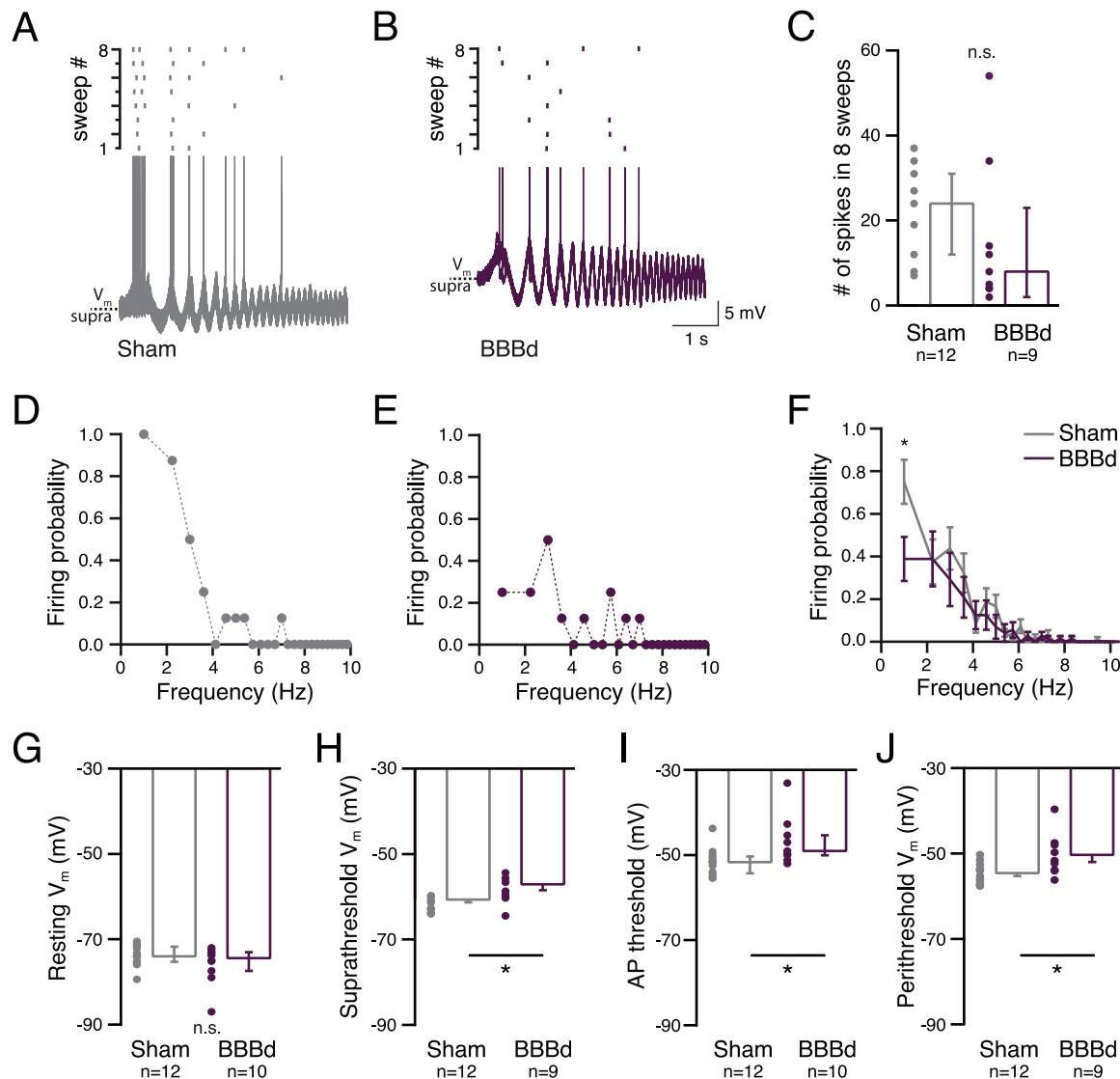
Fig. 6. Hippocampal non-resonant neurons are less excitable in post-stroke epileptogenesis; same analysis as in Fig. 4 but for non-resonant neurons. **A-B.** Overlaid suprathreshold voltage responses (bottom) with marks of the corresponding APs (top) from a sham (A) and a BBBd non-resonant neuron (B). **C.** Total number of spikes out of eight sweeps in sham and BBBd NonRes neurons. **D-E.** Firing probability over frequency from the examples shown in A-B. **F.** Averaged firing probability of sham and BBBd non-resonant neurons. At 1 Hz the firing probability was statistically significant (MW $p = 0.033$). **G-J.** Resting V_m, suprathreshold V_m (t-test $p = 0.041$), AP threshold (MW $p = 0.012$) and perithreshold V_m (t-test $p = 0.036$) of sham and BBBd non-resonant neurons.

simulation vs. 1.01 ± 0.1 experimental (exp.) data) and a second component with a peak at ~1.7 containing Res neurons (30%, 1.68 ± 0.06 simulation vs. 1.71 ± 0.25 exp. data; Fig. 7B left). Histogramming the frequency at Z_{max} revealed a peak at lower frequencies associated with NonRes neurons (f_{Zmax} mean $\pm$ SEM, 0.96 ± 0.07 Hz simulation vs. 0.84 ± 0.15 Hz exp. data), while values associated with Res neurons are distributed between 2 and 7 Hz (f_{Zmax} 4.1 ± 0.2 Hz simulations vs. 4.2 ± 0.6 Hz exp. data; Fig. 7B, right). Accordingly, the impedance profiles obtained at subthreshold potential show a clear difference between both neuronal groups. While NonRes neurons reveal a monotonic decay of impedance as frequency increases, Res neurons show the characteristic impedance reduction for frequencies below 3 and above 8 Hz (Fig. 7C, left). Therefore, simulated neurons reproduce the heterogeneity of Q values and peak impedance frequencies. The phase-lag curves of simulated neurons show as well a difference between both cell populations as experimentally observed, with Res neurons displaying a lower phase-lag for all explored frequencies (Fig. 7C, right). Furthermore, the R_{in} of simulated neurons covers a wide range (50–250 MΩ), finding similar averaged values compared to the experimental data (NonRes $141.6 \pm$

7.0 MΩ vs. 130.4 ± 8.0 MΩ, Res 90.0 ± 7.2 MΩ vs. 89.9 ± 10.1 MΩ, for simulated vs. exp. data).

These results show that our conductance-based simulated population of PCs containing physiologically diverse values for G_M and G_{NaP} is capable of reproducing the range and heterogeneity of intrinsic properties we observed in experimental sham conditions. This supports the idea that the predominant contributors setting resonant behavior of neurons at subthreshold potentials are the intrinsic variabilities of I_M and I_{NaP}, as previously proposed (Vera et al., 2017). Moreover, the fact that we can reproduce the heterogeneous intrinsic parameters by using the natural variability of G_M and G_{NaP} in hippocampal neurons suggests that perhaps a modulation of these conductances, as experimentally described (Astman et al., 1998; Delmas and Brown, 2005; Gorelova and Yang, 2000; Ma et al., 1997; Mantegazza et al., 2005; Moore et al., 1988; Schweitzer, 2000), might underlay the changes observed during post-stroke epileptogenesis. To test this hypothesis, we explored the sensitivity of neuronal excitability to modifications on G_M or G_{NaP} that are expected to increase the population of resonant neurons (Vera et al., 2017), as observed in BBBd. Therefore, we used the same values of the
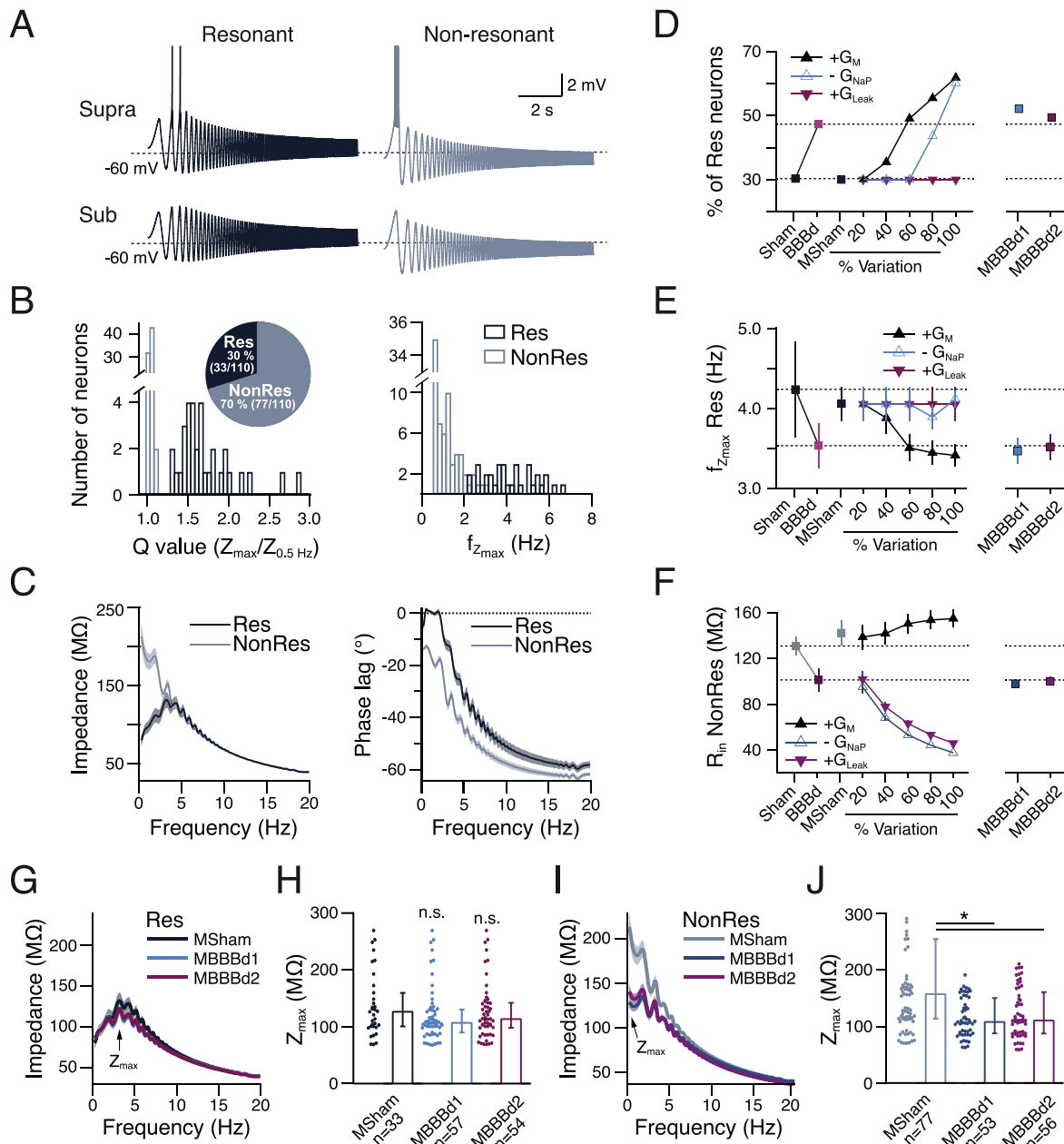
Fig. 7. Modulated subthreshold conductances can explain excitability changes observed in BBBd. A population of CA1 neurons ($n = 110$) was simulated by using different combinations of muscarine-sensitive potassium and persistent sodium conductances (G_M and G_{NaP}) for each particular neuron. **A.** Voltage traces of a Res and NonRes neuron from the simulated population. Neurons were depolarized with constant current until they started firing action potentials (i.e., suprathreshold potential, Supra) when stimulated with the ZAP protocol. Depolarized subthreshold potential (Sub) is 1 pA in holding current below Supra potential. **B.** Histogram of Q values (left, bin = 0.05) and f_{Zmax} (right, bin = 0.2 Hz) from simulated Res ($n = 33$) and NonRes ($n = 77$) neurons. Inset (left) depicts proportions of Res and NonRes neurons. **C.** Impedance profile (left) and phase-lag curves (right) for simulated neurons (mean ± SEM). **D-F.** Quantification of percentage of Res and NonRes neurons (D), f_{Zmax} of Res neurons (E) as well as R_{in} of NonRes neurons (F) for various conductances tested. Sham and BBBd are the experimental data obtained in this study, MSham equals the modeled sham condition. Sensitivity analysis was performed by modulating single conductances in 20% steps, i.e., increase in G_M (black), reduction in G_{NaP} (blue) or increase in G_{Leak} (magenta). The two combinations reproducing best the experimental data were MBBBd1, where the BBBd data was reproduced with 50% increase in G_M in all neurons plus 20% decrease in G_{NaP} of NonRes neurons, and MBBBd2 with 60% increase in G_M in all neurons plus an increase in 23% G_{Leak} in NonRes neurons. **G.** Impedance profile of Res neurons from the three simulated conditions (mean ± SEM). Arrow pointing on the maximal impedance (Z_{max}). **H.** Z_{max} was compared between modeled groups of Res neurons. **I-J.** Impedance profiles and comparison of Z_{max} values for simulated NonRes neurons. (For interpretation of the references to colour in this figure legend, the reader is referred to the web version of this article.)

parameters that describe the modeling of sham condition (MSham) and modified only the maximal conductance of G_M or G_{NaP} in 20% steps (from 20 to 100% change) for each neuron to then evaluate the effect at the population level (Fig. 7D-F).

Increasing G_M produces a rise in the percentage of resonant neurons that starts after a 40% increase, reaching up to ~60% of Res neurons

after a 100% rise in G_M (Fig. 7D). Interestingly, the increase in G_M is associated with a small reduction in f_{Zmax} (Fig. 7E), similar to the trend observed in our experimental data (Fig. 2F). These simulations show that by increasing G_M it is possible to switch NonRes to Res neurons, and, therefore, that an increased G_M is a candidate to drive the changes observed in BBBd. In addition to the modification of resonant properties,

our experimental data show that BBBd also produces a reduction in Z_{max} as well as in R_{in} of NonRes neurons (Fig. 5C-D; Fig. 7F, left). The increase in G_M, however, fails to reproduce this observed drop of R_{in} in NonRes neurons (Fig. 7F, middle), suggesting that G_M alone cannot underlie all the modifications observed in post-stroke epileptogenesis.

In the case of G_{NaP}, it has been proposed that to increase the proportion of Res neurons it has to be reduced (Vera et al., 2017). Therefore, we explored the effect of reducing G_{NaP} in 20% steps. As predicted, we find that reducing G_{NaP} does indeed increase the proportion of Res neurons, reaching up to ~60% of Res neurons when reducing G_{NaP} by 100% (Fig. 7D). However, the increase in the number of Res neurons is not accompanied with a reduction in f_{Zmax} that would further converge experimental data from BBBd Res neurons with our simulations (Figs. 2E & 7E). Additionally, and in contrast to G_M modification, the reduction of G_{NaP} has a strong impact on the R_{in} of all neurons, reproducing the drop observed in BBBd NonRes neurons after only a 20% decrease of G_{NaP} (Fig. 7F), and inducing a reduction of R_{in} in BBBd Res neurons that was not observed experimentally. Therefore, these results suggest that a reduction in G_{NaP} can contribute, but by itself is not sufficient, to drive the changes observed in BBBd.

A third conductance present in hippocampal neurons that could contribute to the reduction in R_{in} that we observed only in BBBd NonRes neurons, is the leak conductance (G_{Leak}) (Schweitzer et al., 1998; Shinohara and Kawasaki, 1997). Leak conductance contributes to set the resting V_m and the R_{in} of cells, controlling cell excitability by producing a constant outward current that has a hyperpolarizing effect on V_m (Goldstein et al., 2001). Therefore, an increase in G_{Leak} would reduce the R_{in} of neurons and potentially influence the perithreshold dynamic that determines whether neurons resonate or not (Prescott et al., 2008; Vera et al., 2017). To test this possibility, we evaluated the effect of increasing G_{Leak} in 20% steps, finding that the proportion of Res neurons and the f_{Zmax} are insensitive to it (Fig. 7D, E). However, similar to the reduction on G_{NaP}, the increase in G_{Leak} has a strong effect on R_{in}, reproducing the drop in BBBd NonRes neurons after a reduction of only 20% (Fig. 7F).

Taking into account the results of our sensitivity analysis, it can be proposed that the changes observed in BBBd can arise as a consequence of several combinations of the studied conductances. Therefore, we explored the minimal mechanisms that could account for most of the changes observed in BBBd, having as landmark observations the increase in the proportion of Res neurons and the drop in R_{in} that occurs only to NonRes neurons (Fig. 5D). We tested several combinations of changes involving G_M, G_{NaP} and G_{Leak} applied to all neurons (Res and NonRes), finding that each time we reduced G_{NaP} or increased G_{Leak}, even with 10%, we always obtained a reduction in the R_{in} of Res neurons (data not shown), being in discrepancy with our BBBd results. This indicates that the approach of modifying G_{NaP} or G_{Leak} globally in all neurons cannot reproduce the BBBd condition, and suggests that the modifications that reduce R_{in} should be directed specifically to NonRes neurons. Therefore, the reduction of G_{NaP} or the increase in G_{Leak} that can reproduce a drop in R_{in} seemed to affect particularly those neurons that did not shift to the Res population under BBBd condition but remained NonRes neurons. Based on this observation we tested whether a two-step mechanism, in which a first step increases G_M in all neurons and a second step reduces the excitability only in NonRes neurons, can account for the changes observed in BBBd. Indeed, by combining a 50% increase in G_M in all neurons and a reduction of 20% G_{NaP} in NonRes neurons (Model MBBBd1) or, by increasing 60% G_M in all neurons and increasing G_{Leak} in 23% in NonRes neurons (Model MBBBd2) it was possible to reproduce the increase in the proportion of Res neurons (Fig. 7D, right), their reduction in f_{Zmax} (Fig. 7E, right, median Q3/Q1, MSham: 3.85 1.10/0.75 vs. MBBBd1: 3.05 1.20/0.50, MW $p = 0.015$, MSham vs. MBBBd2: 3.35 + 0.90/−0.85, MW $p = 0.033$) as well as the drop of R_{in} in NonRes neurons (Fig. 7F, right, median Q3/Q1, MSham: 135.5 56.5/39.5 vs. MBBBd1: 91.5 34.5/17.0, MW $p = 7e^{-6}$, MSham vs. MBBBd2: 92.0 38.5/19.5, MW $p = 4e^{-5}$). Moreover, these two mechanisms also mimicked the decline in phase-lag observed in BBBd NonRes

neurons (median Q3/Q1, MSham: −48.5 13.0/12.5 vs. MBBBd1: −34.0 7.0/13.0, MW $p = 2e^{-5}$, MSham vs. MBBBd2: −37.5 8.5/13.5, MW $p = 0.013$). However, neither of those two-step mechanisms were able to account for the increase in phase-lag observed in Res neurons (see Table 4, MSham vs. MBBBd1, MW $p = 0.44$, MBBBd2 $p = 0.83$), suggesting that there are additional factors that were not contemplated in our simulations. Nevertheless, both two-step mechanisms replicated our experimental data with no changes in the impedance profile and Z_{max} of Res neurons (see Table 4, MSham vs. MBBBd1, MW $p = 0.16$, MBBBd2 $p = 0.46$) and with the reductions in the impedance profile and Z_{max} in NonRes neurons (Fig. 7G-J, median Q3/Q1, MSham: 157.0 97.5/43.0 vs. MBBBd1: 108.0 42.5/20.0, MW $p = 1e^{-5}$, MSham vs. MBBBd2: 110.5 50.0/23.0, MW $p = 4e^{-4}$) that are fundamental properties for determining the resonant behavior.

Taking together, our computer simulations indicate that by modulating subthreshold conductances it is possible to account for most of the changes we found in post-stroke epileptogenesis. While the increase in the proportion of Res neurons can be induced almost exclusively by an increase in G_M, the reduction of excitability observed in NonRes neurons can be produced by either a reduction of G_{NaP} or by an increase in G_{Leak}. Since these two mechanisms are not exclusive to each other, it is possible that modulating both conductances could work together to reduce the excitability of NonRes neurons in BBBd.

4. Discussion

We report on a global remapping of intrinsic properties of hippocampal PCs leading to increased perithreshold theta resonance during the phase of epileptogenesis. We find that i) the proportion of theta-resonant neurons points towards an increase, that ii) Res neurons show an increased phase lag as well as a more hyperpolarized suprathreshold and perithreshold V_m and iii) that NonRes neurons show a reduction in Z_{max} and R_{in} as well as a more depolarized suprathreshold V_m, AP threshold and perithreshold V_m. Using a computer model of the biophysical properties of NonRes and Res neurons, these findings can be explained by a switch in the behavior of neurons from NonRes to Res. Our findings correlate well with our previous observation of an increase in theta power in vivo in epileptogenic rats (Lippmann et al., 2017). Altered resonance behavior is likely to have a severe impact on information processing within theta oscillations and may contribute to epilepsy-related cognitive dysfunctions.

BBBd has previously been suggested as a major cause underlying hippocampal hyperexcitability and network alterations following cortical photothrombosis (Lapilover et al., 2012; Lippmann et al., 2017). However, alternative explanations like increased cystatin c or neuropeptide Y expression (Kharlamov et al., 2007; Pirttilä and Pitkänen, 2006), free radicals or inflammatory responses (Bidmon et al., 1998; Cacheaux et al., 2009; Kharlamov et al., 2007; Nowicka et al., 2008; Schmidt et al., 2015) as well as changes in hippocampal blood flow or propagating abnormal activity from the injury core may also contribute to the observed effects in theta resonance behavior.

Of the many different and sometimes contrasting phenomena linked to epileptogenesis (Noebels et al., 2012), we consider theta activity in general and perithreshold theta resonance in particular highly relevant. It has previously been shown that theta oscillations often precede seizure initiation both in rodents and in humans (Amiri et al., 2019; Karunakaran et al., 2016; Kuo et al., 2018). Enhanced theta resonance behavior may favor abnormal network synchronization and, thereby, may ultimately contribute to epileptic seizures. It remains to be investigated whether perithreshold theta resonance is also affected in chemical- or stimulus-induced epilepsy models, for which theta oscillations were shown to undergo either decreases (Chauvière et al., 2009; Dugladze et al., 2007; Kilias et al., 2018) or increases (Broggini et al., 2016; Kitchigina and Butuzova, 2009) in power, frequency, and phase coupling. However, we consider the model of BBBd-associated epileptogenesis as being closest to how most patients develop acquired

Table 4

Simulated intrinsic electrophysiological properties for modeled sham (MSham) and BBBd condition (MBBBd). MBBBd was modeled based on MSham values by increasing G_M plus either reducing G_{NaP} (MBBBd1) or increasing G_{Leak} (MBBBd2). Same analysis and parameters as presented in Table 3 for subthreshold V_m calculated using computer simulations. Values given as mean ± SEM, *indicates statistical significance, statistical data relevant to Fig. 7 are described in the main text.

Res	n	V_m(mV)		R_{in}(MΩ)		Z_{max}(MΩ)		Q value		f_{Zmax}(Hz)		Φ_{6Hz}(°)		Φ_{fZmax}(°)	
MSham	33	−59.0	± 0.0	90.0	± 7.0	138.0	± 10.0	1.68	± 0.05	4.1	± 0.20	−37.0	± 3.0	−21.5	± 1.0
MBBBd1	57	−59.0	± 0.0	85.5	± 4.5	121.0	± 6.5	1.45	± 0.05*	3.5	± 0.15*	−34.0	± 2.0	−17.0	± 1.0*
MBBBd2	54	−59.0	± 0.0	89.0	± 5.0	126.5	± 7.0	1.47	± 0.05*	3.5	± 0.15*	−35.5	± 2.0	−17.5	± 1.0*
NonRes	**n**	**V_m(mV)**		**R_{in}(MΩ)**		**Z_{max}(MΩ)**		**Q value**		**f_{Zmax}(Hz)**		**Φ_{6Hz}(°)**		**Φ_{fZmax}(°)**	
MSham	77	−60.0	± 0.0	141.5	± 7.0	192.5	± 13.0	1.01	± 0.00	1.0	± 0.10	−46.5	± 2.0	−13.5	± 1.0
MBBBd1	53	−59.5	± 0.0*	97.5	± 4.0*	116.0	± 5.0*	1.04	± 0.00*	1.8	± 0.10*	−35.5	± 1.5*	−9.5	± 0.5*
MBBBd2	56	−59.5	± 0.0*	99.5	± 4.5*	123.5	± 6.0*	1.03	± 0.00*	1.5	± 0.10*	−39.0	± 1.5*	−10	± 0.5

epilepsies because it mechanistically mirrors brain diseases like stroke, trauma, tumors or infections, which often result into epilepsy (Friedman et al., 2009; Herman, 2002; Pitkänen et al., 2015; Shlosberg et al., 2010).

Mechanistically, the role of individual PCs in theta oscillations is determined, at least in part, by their intrinsic resonance behavior (Buzsáki, 2002; Hutcheon and Yarom, 2000). Four currents mediated by specific channels are known to play important roles in subthreshold excitability: the hyperpolarization-activated and cyclic nucleotide-gated cation current, I_h, the muscarinic potassium current, I_M, the persistent sodium current, I_{NaP}, and the unspecific leak current, I_{Leak} (Hu et al., 2002; Hutcheon and Yarom, 2000; Vera et al., 2017). I_h-mediated subthreshold resonance is expressed at hyperpolarized potentials in all PCs and is involved in low-frequency filtering and synchronization of synaptic inputs (Hu et al., 2009; Magee, 1998; Vaidya and Johnston, 2013). However, I_h has been shown not to be essential for generating theta oscillations (Nolan et al., 2004). In contrast, I_M and I_{NaP} are crucial for perithreshold theta resonance by modulating cellular excitability by, e. g., implementing bandpass filter properties (Gutfreund et al., 1995). Further on, I_M and I_{NaP} determine whether resonant mechanisms influence action potential firing (Vera et al., 2017) supporting the entrainment as well as phase-coupling of theta oscillations (Cobb et al., 1995). In addition, I_{Leak} decreases R_{in} and therewith reduces neuronal excitability favoring the expression of perithreshold resonance behavior. Importantly, at perithreshold potentials only a minor fraction of PCs behaves as resonant neurons (Vera et al., 2017). These neurons will pass their preferred frequency (theta) towards downstream neurons, ultimately contributing to theta network oscillations (Richardson et al., 2003). Non-resonant neurons, on the other hand, act as lowpass filters and do not contribute actively towards theta activity. Therefore, the proportion and excitability of Res and NonRes neurons is fundamental for the strength and duration of theta oscillations.

Our computational model shows that modifications in the strength of the conductances G_M, G_{NaP} as well as G_{Leak} are able to rearrange PC excitability, shifting NonRes towards Res neurons and offering a mechanism to explain the increment in hippocampal theta resonance observed in post-stroke epileptogenesis (Lippmann et al., 2017). While particularly a rise in G_M increases resonant drive in NonRes neurons, converting some of them to Res neurons, a reduction in G_{NaP} or an increase in G_{Leak} may account for the observed drop in R_{in} of NonRes neurons. While I_M acts as a resonator by directly filtering low-frequency inputs, together with I_{Leak} it also dampens cell excitability and therefore firing probability (Goldstein et al., 2001; Hu et al., 2009; Vera et al., 2017; Verneuil et al., 2020). In contrast, I_{NaP} amplifies voltage responses and drives neurons towards the AP threshold (Vera et al., 2017; Verneuil et al., 2020).

From previous work and from the present data, it is conceivable that I_M, I_{NaP} and/or I_{Leak} represent promising targets for therapeutic intervention or even prevention of epileptogenesis. However, it remains open whether the observed changes in perithreshold theta resonance behavior represent a *dysfunction* that contributes towards epileptogenesis or whether they represent a *homeostatic* reaction of the neuronal network to counteract other, detrimental mechanisms of epileptogenesis (Wolfart and Laker, 2015). Regarding the possibility of a homeostatic compensation, one key player modulating the balance of I_M, I_{NaP} and I_{Leak} in the hippocampus is the cholinergic system. In the healthy brain acetylcholine may promote theta oscillations (Buzsáki, 2002; Dannenberg et al., 2017; Teitelbaum et al., 1975) by suppressing I_M (Brown and Passmore, 2009; Halliwell and Adams, 1982) as well as I_{Leak} (Benson et al., 1988; Madison et al., 1987) and by enhancing I_{NaP} at perithreshold V_m (Carrillo-Reid et al., 2009; Yamada-Hanff and Bean, 2013), but see (Cantrell et al., 1996; Mittmann and Alzheimer, 1998). However, in hyperexcitable extracellular solutions as well as epileptic conditions neural networks develop an increased sensitivity for cholinergic activation (Friedman et al., 2007; Williams and Kauer, 1997; Zimmerman et al., 2008). With this increased sensitivity acetylcholine would be able to

further activate I_{NaP} as well as suppress I_M and I_{Leak}, ultimately driving neurons towards their AP threshold and transforming network oscillations into epileptic activity. A homeostatic downregulation of the cholinergic system counteracting the epileptogenicity has previously been shown in chemical-induced epileptic rodents (Gnatek et al., 2012; Kaufer et al., 1998; Maslarova et al., 2013; Zimmerman et al., 2008). Therefore, it could be expected that an overcompensated (i.e., reduced) cholinergic input to PCs will enhance I_M contributing to increase the fraction of Res neurons. Additionally, this reduced cholinergic input could also decrease I_{NaP} and/or increase I_{Leak} selectively in NonRes neurons. This could, according to our model, explain the reduction in R_{in} observed only in NonRes neurons. Although differential changes observed in Res and NonRes neurons are not yet clarified, it has been described that subpopulations of PCs in the hippocampus (Graves et al., 2012; Yamada-Hanff and Bean, 2013) show differential sensitivity to cholinergic modulation. The present changes in intrinsic properties in post-stroke epileptogenesis and the observation that no major cell loss occurs in CA1 after cortical photothrombosis (Kharlamov et al., 2007) suggest a unilateral transformation of NonRes neurons to Res neurons, while Res neurons may remain unchanged. However, data from Res neurons are affected by the 'newcomers' that could explain their changes in phase lag as well as in excitability.

Although the network may compensate for a cholinergic hyperexcitability, an epileptogenic development may still advance due to other processes, e.g., a reduced cholinergic anti-inflammatory response (Gnatek et al., 2012) or BBBd-induced excitatory synaptogenesis (Weissberg et al., 2015). All in all, epileptogenesis may lead to an increased cholinergic sensitivity with a subsequent overcompensation targeting specifically NonRes neurons. Therefore, NonRes neurons may transform into Res neurons contributing towards an increased theta network activity.

In the context of homeostatic compensation it is also interesting to consider the effects of anti-epileptic drugs that were shown to either inhibit I_{NaP} like phenytoin, carbamazepine, or valproate (Colombo et al., 2013; Sun et al., 2007; Taverna et al., 1998) or preserve I_M, like valproate or retigabine (Cooper, 2001; Kay et al., 2015). All these drugs effectively attenuate seizures but are also known to impair learning and memory (Ijff and Aldenkamp, 2013; Zwierzyńska et al., 2017). Indeed, it has been shown that phenytoin, carbamazepine as well as valproate increased the power of theta network activity (Besser et al., 1992; Salinsky et al., 2004; Segura-Bruna et al., 2006) and, thereby potentially contribute towards impaired learning and memory. In view of the well-established pharmacological profile of anti-epileptic drugs, it is conceivable that the changes in intrinsic properties of PCs we observed mirror an attempt of the hippocampal network to homeostatically compensate for the growing hyperexcitability and epileptogenicity by reducing the cholinergic tone. Long-term in vivo recordings combined with pharmacological interventions will be required to address this hypothesis in future experiments. Independent on a beneficial or detrimental role of increased theta resonance, our data provides evidence for a link between the intrinsic resonance behavior of hippocampal PCs and epileptogenesis.

In conclusion, our work suggests that post-stroke epileptogenesis is associated with a rearrangement of the intrinsic excitability across hippocampal pyramidal cells at perithreshold potential that is seen as an increased proportion and excitability of resonant neurons together with a decreased proportion and excitability of non-resonant neurons. We propose that this remapping of perithreshold excitability may be caused by a global change related to the epileptogenic state that switches non-resonant to resonant neurons. Enhanced theta resonance would enable neurons to communicate their preferred theta frequency downstream to postsynaptic neurons strengthening theta network activity. This pathologic increased theta network activity could severely influence information processing and promote epilepsy-related cognitive dysfunctions.

Author contributions

JV and KL designed the study, performed the experiments, analyzed the data and wrote the manuscript. JV performed computer simulations.

Declaration of Competing Interest

None.

References

Abbott, N.J., Rönnbäck, L., Hansson, E., 2006. Astrocyte – endothelial interactions at the blood – brain barrier. Nat. Neurosci. Rev. 7, 41–53. https://doi.org/10.1038/nrn1824.

Adams, P.R., Brown, D.A., Constanti, A., 1982. M-currents and other potassium currents in bullfrog sympathetic neurones. J. Physiol. 330, 537–572. https://doi.org/10.1113/jphysiol.1982.sp014357.

Amiri, M., Frauscher, B., Gotman, J., 2019. Interictal coupling of HFOs and slow oscillations predicts the seizure-onset pattern in mesiotemporal lobe epilepsy. Epilepsia 60, 1160–1170. https://doi.org/10.1111/epi.15541.

Astman, N., Gutnick, M.J., Fleidervish, I.A., 1998. Activation of protein kinase c increases neuronal excitability by regulating persistent Na+ current in mouse neocortical slices. J. Neurophysiol. 80, 1547–1551. https://doi.org/10.1152/jn.1998.80.3.1547.

Benson, B.Y.D.M., Blitzer, R.D., Landaut, E.M., 1988. An analysis of the depolarization produced in guinea-pig hippocampus by cholinergic receptor stimulation. Physiology 404, 479–496.

Besser, R., Hornung, K., Theisohn, M., Rothacher, G., Krämer, G., 1992. EEG changes in patients during the introduction of carbamazepine. Electroencephalogr. Clin. Neurophysiol. 83, 19–23. https://doi.org/10.1016/0013-4694(92)90128-5.

Bidmon, H.J., Kato, K., Schleicher, A., Witte, O.W., Zilles, K., 1998. Transient increase of manganese-superoxide dismutase in remote brain ares focal photothrombotic cortical lesion. Stroke 29, 203–211. https://doi.org/10.1161/01.STR.29.1.203.

Broggini, A.C.S., Esteves, I.M., Romcy-Pereira, R.N., Leite, J.P., Leão, R.N., 2016. Pre-ictal increase in theta synchrony between the hippocampus and prefrontal cortex in a rat model of temporal lobe epilepsy. Exp. Neurol. 279, 232–242. https://doi.org/10.1016/j.expneurol.2016.03.007.

Brown, D.A., Passmore, G.M., 2009. Neural KCNQ (Kv7) channels. Br. J. Pharmacol. 156, 1185–1195. https://doi.org/10.1111/j.1476-5381.2009.00111.x.

Buzsáki, G., 2002. Theta oscillations in the hippocampus. Neuron 33, 325–340. https://doi.org/10.1016/S0896-6273(02)00586-X.

Buzsáki, G., 2015. Hippocampal sharp wave-ripple: a cognitive biomarker for episodic memory and planning. Hippocampus 25, 1073–1188. https://doi.org/10.1002/hipo.22488.

Cacheaux, L.P., Ivens, S., David, Y., Lakhter, A.J., Bar-Klein, G., Shapira, M., Heinemann, U., Friedman, A., Kaufer, D., 2009. Transcriptome profiling reveals TGF-ß signaling involvement in epileptogenesis. J. Neurosci. 29, 8927–8935. https://doi.org/10.1523/JNEUROSCI.0430-09.2009.

Cantrell, A.R., Ma, J.Y., Scheuer, T., Catterall, W.A., 1996. Muscarinic modulation of sodium current by activation of protein kinase C in rat hippocampal neurons. Neuron 16, 1019–1026. https://doi.org/10.1016/S0896-6273(00)80125-7.

Carrillo-Reid, L., Tecuapetla, F., Vautrelle, N., Hernández, A., Vergara, R., Galarraga, E., Bargas, J., 2009. Muscarinic enhancement of persistent sodium current synchronizes striatal medium spiny neurons. J. Neurophysiol. 102, 682–690. https://doi.org/10.1152/jn.00134.2009.

Casanova, J.R., Nishimura, M., Swann, J.W., 2014. The effects of early-life seizures on hippocampal dendrite development and later-life learning and memory. Brain Res. Bull. 103, 39–48. https://doi.org/10.1016/j.brainresbull.2013.10.004.

Chauvière, L., Rafrafi, N., Thinus-blanc, C., Bartolomei, F., Esclapez, M., Bernard, C., 2009. Early deficits in spatial memory and theta rhythm in experimental temporal lobe epilepsy. J. Neurosci. 29, 5402–5410. https://doi.org/10.1523/JNEUROSCI.4699-08.2009.

Cobb, S.R., Buhl, E.H., Halasy, K., Paulsen, O., Somogyi, P., 1995. Synchronization of neuronal activity in hippocampus by individual GABAergic interneurons. Nature 378, 75–78.

Colombo, E., Franceschetti, S., Avanzini, G., Mantegazza, M., 2013. Phenytoin inhibits the persistent sodium current in neocortical neurons by modifying its inactivation properties. PLoS One 8, e55329. https://doi.org/10.1371/journal.pone.0055329.

Cooper, E.C., 2001. Potassium channels: how genetic studies of epileptic syndromes open paths to new therapeutic targets and drugs. Epilepsia 42, 49–54. https://doi.org/10.1046/j.1528-1157.2001.0420s5049.x.

Dannenberg, H., Young, K., Hasselmo, M., 2017. Modulation of hippocampal circuits by muscarinic and nicotinic receptors. Front. Neural. Circuits. 11, 1–18. https://doi.org/10.3389/fncir.2017.00102.

Dell, R.B., Holleran, S., Ramakrishnan, R., 2002. Sampel Size Determination. ILAR J. 43, 207–213.

Delmas, P., Brown, D.A., 2005. Pathways modulating neural KCNQ/M (Kv7) potassium channels. Nat. Rev. Neurosci. https://doi.org/10.1038/nrn1785.

Dugladze, T., Vida, I., Tort, A.B., Gross, A., Otahal, J., Heinemann, U., Kopell, N.J., Gloveli, T., 2007. Impaired hippocampal rhythmogenesis in a mouse model of mesial temporal lobe epilepsy. Proc. Natl. Acad. Sci. U. S. A. 104, 17530–17535. https://doi.org/10.1073/pnas.0708301104.

French, C.R., Sah, P., Bucketr, K.J., Gage, P.W., 1990. A voltage-dependent persistent sodium current in mammalian hippocampal neurons. J. Gen. Physiol. 95, 1139–1157. https://doi.org/10.1085/jgp.95.6.1139.

Friedman, A., Behrens, C.J., Heinemann, U., 2007. Cholinergic dysfunction in temporal lobe epilepsy. Epilepsia 48, 126–130. https://doi.org/10.1111/j.1528-1167.2007.01300.x.

Friedman, A., Kaufer, D., Heinemann, U., 2009. Blood-brain barrier breakdown-inducing astrocytic transformation: novel targets for the prevention of epilepsy. Epilepsy Res. 85, 142–149. https://doi.org/10.1016/j.eplepsyres.2009.03.005.

Gnatek, Y., Zimmerman, G., Goll, Y., Najami, N., Soreq, H., Friedman, A., 2012. Acetylcholinesterase loosens the brain's cholinergic anti-inflammatory response and promotes epileptogenesis. Front. Mol. Neurosci. 5, 66. https://doi.org/10.3389/fnmol.2012.00066.

Goldstein, S.A.N., Bockenhauer, D., O'Kelly, I., Zilberberg, N., 2001. Potassium leak channels and the KCNK family of two-p-domain subunits. Nat. Rev. Neurosci. 2, 175–184. https://doi.org/10.1038/35058574.

Golowasch, J., Thomas, G., Taylor, A.L., Patel, A., Pineda, A., Khalil, C., Nadim, F., 2009. Membrane capacitance measurements revisited: dependence of capacitance value on measurement method in nonisopotential neurons. J. Neurophysiol. 102, 2161–2175. https://doi.org/10.1152/jn.00160.2009.

Gorelova, N.A., Yang, C.R., 2000. Dopamine D1/D5 receptor activation modulates a persistent sodium current in rat prefrontal cortical neurons in vitro. J. Neurophysiol. 84, 75–87. https://doi.org/10.1152/jn.2000.84.1.75.

Graves, A.R., Moore, S.J., Bloss, E.B., Mensh, B.D., Kath, W.L., Spruston, N., 2012. Hippocampal pyramidal neurons comprise two distinct cell types that are countermodulated by metabotropic receptors. Neuron 76, 776–789. https://doi.org/10.1016/j.neuron.2012.09.036.

Gutfreund, Y., Yarom, Y., Segev, I., 1995. Subthreshold oscillations and resonant frequency in guinea-pig cortical neurons: physiology and modelling. J. Physiol. 483, 621–640. https://doi.org/10.1113/jphysiol.1995.sp020611.

Halliwell, J.V., Adams, P.R., 1982. Voltage-clamp analysis of muscarinic excitation in hippocampal neurons. Brain Res. 250, 71–92. https://doi.org/10.1016/0006-8993(82)90954-4.

Herman, S.T., 2002. Epilepsy after brain insult: targeting epileptogenesis. Neurology 59, S21–S26.

Hodgkin, A.L., Huxley, A.F., 1952. A quantitative description of membrane current and its application to conduction and excitation in nerve. J. Physiol. 117, 500–544.

Hu, H., Vervaeke, K., Storm, J.F., 2002. Two forms of electrical resonance at theta frequencies, generated by M-current, h-current and persistent Na+ current in rat hippocampal pyramidal cells. J. Physiol. 545, 783–805. https://doi.org/10.1113/jphysiol.2002.029249.

Hu, H., Vervaeke, K., Graham, L.J., Storm, J.F., 2009. Complementary theta resonance filtering by two spatially segregated mechanisms in CA1 hippocampal pyramidal neurons. J. Neurosci. 29, 14472–14483. https://doi.org/10.1523/JNEUROSCI.0187-09.2009.

Hutcheon, B., Yarom, Y., 2000. Resonance, oscillation and the intrinsic frequency preferences of neurons. Trends Neurosci. 23, 216–222. https://doi.org/10.1016/S0166-2236(00)01547-2.

Hutcheon, B., Miura, R.M., Puil, E., 1996. Subthreshold membrane resonance in neocortical neurons. J. Neurophysiol. 76, 683–697.

Ijff, D.M., Aldenkamp, A.P., 2013. Cognitive side-effects of antiepileptic drugs in children. Handb. Clin. Neurol. 111, 707–718. https://doi.org/10.1016/B978-0-444-52891-9.00073-7.

Karunakaran, S., Grasse, D.W., Moxon, K.A., 2016. Role of CA3 theta-modulated interneurons during the transition to spontaneous seizures. Exp. Neurol. 283, 341–352. https://doi.org/10.1016/j.expneurol.2016.06.027.

Kaufer, D., Friedman, A., Seidman, S., Soreq, H., 1998. Acute stress facilitates long-lasting changes in cholinergic gene expression. Nature 393, 373–377. https://doi.org/10.1038/30741.

Kay, H.Y., Greene, D.L., Kang, S., Kosenko, A., Hoshi, N., 2015. M-current preservation contributes to anticonvulsant effects of valproic acid. J. Clin. Invest. 125, 3904–3914. https://doi.org/10.1172/JCI79727.

Kharlamov, E.A., Kharlamov, A., Kelly, K.M., 2007. Changes in neuropeptide Y protein expression following photothrombotic brain infarction and epileptogenesis. Brain Res. 1127, 151–162. https://doi.org/10.1016/j.brainres.2006.09.107.

Kilias, A., Häussler, U., Heining, K., Froriep, U.P., Haas, C.A., Egert, U., 2018. Theta frequency decreases throughout the hippocampal formation in a focal epilepsy model. Hippocampus 28, 375–391. https://doi.org/10.1002/hipo.22838.

Kim, S.Y., Senatorov, V.V., Morrissey, C.S., Lippmann, K., Vazquez, O., Milikovsky, D.Z., Gu, F., Parada, I., Prince, D.A., Becker, A.J., Heinemann, U., Friedman, A., Kaufer, D., 2017. TGFβ signaling is associated with changes in inflammatory gene expression and perineuronal net degradation around inhibitory neurons following various neurological insults. Sci. Rep. 7, 1–14. https://doi.org/10.1038/s41598-017-07394-3.

Kitchigina, V.F., Butuzova, M.V., 2009. Theta activity of septal neurons during different epileptic phases: the same frequency but different significance? Exp. Neurol. 216, 449–458. https://doi.org/10.1016/j.expneurol.2009.01.001.

Koch, C., 1984. Cable theory in neurons with active, linearized membranes. Biol. Cybern. 50, 15–33. https://doi.org/10.1007/BF00317936.

Kuo, C.-C., Tucker, D.M., Luu, P., Jenson, K., Tsai, J.J., Ojemann, J.G., Holmes, M.D., 2018. EEG source imaging of epileptic activity at seizure onset. Epilepsy Res. 146, 160–171. https://doi.org/10.1016/j.eplepsyres.2018.07.006.

Lapilover, E.G., Lippmann, K., Salar, S., Maslarova, A., Dreier, J.P., Heinemann, U., Friedman, A., 2012. Peri-infarct blood-brain barrier dysfunction facilitates induction of spreading depolarization associated with epileptiform discharges. Neurobiol. Dis. 48, 495–506.

Lippmann, K., Kaminsky, L., Kim, S.Y., Lublinsky, S., Prager, O., Nichtweiss, J.F., Salar, S., Kaufer, D., Heinemann, U., Friedman, A., 2017. Epileptiform activity and spreading depolarization in the blood-brain barrier-disrupted peri-infarct hippocampus are associated with impaired GABAergic inhibition and synaptic plasticity. J. Cereb. Blood Flow Metab. 37, 1803–1819. https://doi.org/10.1177/0271678X16652631.

Ma, J.Y., Catterall, W.A., Scheuer, T., 1997. Persistent sodium currents through brain sodium channels induced by G protein βγ subunits. Neuron 19, 443–452. https://doi.org/10.1016/S0896-6273(00)80952-6.

Madison, D.V., Lancaster, B., Nicoll, R.A., 1987. Voltage clamp analysis of cholinergic action in the hippocampus. J. Neurosci. 7, 733–741. https://doi.org/10.1523/jneurosci.07-03-00733.1987.

Magee, J.C., 1998. Dendritic hyperpolarization-activated currents modify the integrative properties of hippocampal CA1 pyramidal neurons. J. Neurosci. 18, 7613–7624. https://doi.org/10.1523/jneurosci.18-19-07613.1998.

Mantegazza, M., Yu, F.H., Powell, A.J., Clare, J.J., Catterall, W.A., Scheuer, T., 2005. Molecular determinants for modulation of persistent sodium current by G-protein betagamma subunits. J. Neurosci. 25, 3341–3349. https://doi.org/10.1523/JNEUROSCI.0104-05.2005.

Maslarova, A., Salar, S., Lapilover, E., Friedman, A., Veh, R.W., Heinemann, U., 2013. Increased susceptibility to acetylcholine in the entorhinal cortex of pilocarpine-treated rats involves alterations in KCNQ channels. Neurobiol. Dis. 56, 14–24. https://doi.org/10.1016/j.nbd.2013.02.016.

Mattson, M.P., Guthrie, P.B., Kater, S.B., 1989. Intrinsic factors in the selective vulnerability of hippocampal pyramidal neurons. Prog. Clin. Biol. Res. 317, 333–351.

Mittmann, T., Alzheimer, C., 1998. Muscarinic inhibition of persistent Na+ current in rat neocortical pyramidal neurons. J. Neurophysiol. 79, 1579–1582.

Moore, S.D., Madamba, S.G., Joëls, M., Siggins, G.R., 1988. Somatostatin augments the M-current in hippocampal neurons. Science 239, 278–280. https://doi.org/10.1126/science.2892268.

Neher, E., 1992. Correction for liquid junction potentials in patch clamp experiments. Methods Enzymol. 207, 123–131.

Neuwelt, E.A., 2004. Mechanisms of disease: the blood-brain barrier. Neurosurgery 54, 131–142. https://doi.org/10.1227/01.NEU.0000097715.11966.8E.

Noebels, J.L., Avoli, M., Rogawski, M.A., Olsen, R.W., Delgado-Escueta, A.V., 2012. Jasper's Basic Mechanisms of the Epilepsies, 4th ed. National Center for Biotechnology Information (US), Bethesda. https://doi.org/10.1111/j.1528-1167.2010.02793.x.

Nolan, M., Malleret, G., Dudman, J., Buhl, D., Santoro, B., Gibbs, E., Vronovskaya, S., Buzsaki, G., Siegelbaum, S., Kandel, E., Morozov, A., 2004. A behavioral role for dendritic integration: HCN1 channels constrain spatial memory and plasticity at inputs to distal dendrites of CA1 pyramidal neurons. Cell 119, 719–732. https://doi.org/10.1016/j.cell.2004.11.020.

Nowicka, D., Rogozinska, K., Aleksy, M., Witte, O.W., Skangiel-Kramska, J., 2008. Spatiotemporal dynamics of astroglial and microglial responses after photothrombotic stroke in the rat brain. Acta Neurobiol. Exp. (Wars) 68, 155–168.

Pirttilä, T.J., Pitkänen, A., 2006. Cystatin C expression is increased in the hippocampus following photothrombotic stroke in rat. Neurosci. Lett. 395, 108–113. https://doi.org/10.1016/j.neulet.2005.10.091.

Pitkänen, A., Lukasiuk, K., Dudek, F.E., Staley, K.J., 2015. Epileptogenesis. Cold Spring Harb. Perspect. Med. 5, 1–18.

Prescott, S.A., Ratté, S., De Koninck, Y., Sejnowski, T.J., 2008. Pyramidal neurons switch from integrators in vitro to resonators under in vivo-like conditions. J. Neurophysiol. 100, 3030–3042. https://doi.org/10.1152/jn.90634.2008.

Puil, E., Gimbarzevsky, B., Miura, R.M., 1986. Quantification of membrane properties of trigeminal root ganglion neurons in guinea pigs. J. Neurophysiol. 55, 995–1016.

Richardson, M.J.E., Brunel, N., Hakim, V., 2003. From subthreshold to firing-rate resonance. J. Neurophysiol. 89, 2538–2554. https://doi.org/10.1152/jn.00955.2002.

Rotstein, H.G., 2014. Frequency preference response to oscillatory inputs in two-dimensional neural models: a geometric approach to subthreshold amplitude and

phase resonance. J. Math. Neurosci. 4, 11. https://doi.org/10.1186/2190-8567-4-11.

Salinsky, M.C., Spencer, D.C., Oken, B.S., Storzbach, D., 2004. Effects of oxcarbazepine and phenytoin on the EEG and cognition in healthy volunteers. Epilepsy Behav. 5, 894–902. https://doi.org/10.1016/j.yebeh.2004.07.011.

Schmidt, A., Diederich, K., Strecker, J.K., Geng, B., Hoppen, M., Duning, T., Schäbitz, W. R., Minnerup, J., 2015. Progressive cognitive deficits in a mouse model of recurrent photothrombotic stroke. Stroke 46, 1127–1131. https://doi.org/10.1161/STROKEAHA.115.008905.

Schoknecht, K., Prager, O., Vazana, U., Kamintsky, L., Harhausen, D., Zille, M., Figge, L., Chassidim, Y., Schellenberger, E., Kovács, R., Heinemann, U., Friedman, A., 2014. Monitoring stroke progression: in vivo imaging of cortical perfusion, blood-brain barrier permeability and cellular damage in the rat photothrombosis model. J. Cereb. Blood Flow Metab. 34, 1791–1801. https://doi.org/10.1038/jcbfm.2014.147.

Schweitzer, P., 2000. Cannabinoids decrease the K+ M-current in hippocampal CA1 neurons. J. Neurosci. 20, 51–58. https://doi.org/10.1523/jneurosci.20-01-00051.2000.

Schweitzer, P., Madamba, S.G., Siggins, G.R., 1998. Somatostatin increases a voltage-insensitive K+ conductance in rat CA1 hippocampal neurons. J. Neurophysiol. 79, 1230–1238. https://doi.org/10.1152/jn.1998.79.3.1230.

Segura-Bruna, N., Rodriguez-Campello, A., Puente, V., Roquer, J., 2006. Valproate-induced hyperammonemic encephalopathy. Acta Neurol. Scand. 114, 1–7. https://doi.org/10.1111/j.1600-0404.2006.00655.x.

Shinohara, S., Kawasaki, K., 1997. Electrophysiological changes in rat hippocampal pyramidal neurons produced by cholecystokinin octapeptide. Neuroscience 78, 1005–1016. https://doi.org/10.1016/s0306-4522(96)00653-7.

Shlosberg, D., Benifla, M., Kaufer, D., Friedman, A., 2010. Blood-brain barrier breakdown as a therapeutic target in traumatic brain injury. Nat. Rev. Neurol. 6, 393–403. https://doi.org/10.1038/nrneurol.2010.74.

Spain, W.J., Schwindt, P.C., Crill, W.E., 1987. Anomalous rectification in neurons from cat sensorimotor cortex in vitro. J. Neurophysiol. 57, 1555–1576. https://doi.org/10.1152/jn.1987.57.5.1555.

Sun, G.C., Werkman, T.R., Battefeld, A., Clare, J.J., Wadman, W.J., 2007. Carbamazepine and topiramate modulation of transient and persistent sodium currents studied in HEK293 cells expressing the Nav1.3 α-subunit. Epilepsia 48, 774–782. https://doi.org/10.1111/j.1528-1167.2007.01001.x.

Swann, J.W., Al-Noori, S., Jiang, M., Lee, C.L., 2000. Spine loss and other dendritic abnormalities in epilepsy. Hippocampus 10, 617–625. https://doi.org/10.1002/1098-1063(2000)10:5<617::AID-HIPO13>3.0.CO;2-R.

Taverna, S., Mantegazza, M., Franceschetti, S., Avanzini, G., 1998. Valproate selectively reduces the persistent fraction of Na+ current in neocortical neurons. Epilepsy Res. 32, 304–308. https://doi.org/10.1016/S0920-1211(98)00060-6.

Teitelbaum, H., Lee, J.F., Johannessen, J.N., 1975. Behaviorally evoked hippocampal theta waves: a cholinergic response. Science 188, 1114–1116. https://doi.org/10.1126/science.175440.

Vaidya, S.P., Johnston, D., 2013. Temporal synchrony and gamma-to-theta power conversion in the dendrites of CA1 pyramidal neurons. Nat. Neurosci. 16, 1812–1820. https://doi.org/10.1038/nn.3562.

Valero, M., Averkin, R.G., Fernandez-Lamo, I., Aguilar, J., Lopez-Pigozzi, D., Brotons-Mas, J.R., Cid, E., Tamas, G., Menendez de la Prida, L., 2017. Mechanisms for selective single-cell reactivation during offline sharp-wave ripples and their distortion by fast ripples. Neuron 94, 1234–1247. https://doi.org/10.1016/j.neuron.2017.05.032.

Vera, J., Alcayaga, J., Sanhueza, M., 2017. Competition between persistent Na+ and muscarine-sensitive K+ currents shapes perithreshold resonance and spike tuning in CA1 pyramidal neurons. Front. Cell. Neurosci. 11, 61. https://doi.org/10.3389/fncel.2017.00061.

Vera, J., Pereira, U., Reynaert, B., Bacigalupo, J., Sanhueza, M., 2020. Modulation of frequency preference in heterogeneous populations of theta-resonant neurons. Neuroscience 426, 13–32. https://doi.org/10.1016/j.neuroscience.2019.10.054.

Vera, Jorge, Pezzoli, Maurizio, Pereira, Ulises, Bacigalupo, Juan, Sanhueza, Magdalena, 2014. Electrical resonance in the θ frequency range in olfactory amygdala neurons. PLoS One 9 (1), e85826. https://doi.org/10.1371/journal.pone.0085826.

Verneuil, J., Brocard, C., Trouplin, V., Villard, L., Peyronnet-Roux, J., Brocard, F., 2020. The M-current works in tandem with the persistent sodium current to set the speed of locomotion. PLoS Biol. https://doi.org/10.1371/journal.pbio.3000738.

Watson, B.D., Dietrich, W.D., Busto, R., Wachtel, M.S., Ginsberg, M.D., 1984. Induction of reproducible brain infarction by photochemically initiated thrombosis. Ann. Neurol. 17, 497–504.

Weissberg, I., Wood, L., Kamintsky, L., Vazquez, O., Milikovsky, D.Z., Alexander, A., Oppenheim, H., Ardizzone, C., Becker, A., Frigerio, F., Vezzani, A., Buckwalter, M.S., Huguenard, J.R., Friedman, A., Kaufer, D., 2015. Albumin induces excitatory synaptogenesis through astrocytic TGF-ß/ALK5 signaling in a model of acquired epilepsy following blood-brain barrier dysfunction. Neurobiol. Dis. 78, 115–125. https://doi.org/10.1016/j.nbd.2015.02.029.

Williams, J.H., Kauer, J.A., 1997. Properties of carbachol-induced oscillatory activity in rat hippocampus. J. Neurophysiol. 78, 2631–2640. https://doi.org/10.1152/jn.1997.78.5.2631.

Wolfart, J., Laker, D., 2015. Homeostasis or channelopathy? Acquired cell type-specific ion channel changes in temporal lobe epilepsy and their antiepileptic potential. Front. Physiol. 6, 168. https://doi.org/10.3389/fphys.2015.00168.

Yamada-Hanff, J., Bean, B.P., 2013. Persistent sodium current drives conditional pacemaking in CA1 pyramidal neurons under muscarinic stimulation. J. Neurosci. 33, 15011–15021. https://doi.org/10.1523/jneurosci.0577-13.2013.

Zimmerman, G., Njunting, M., Ivens, S., Tolner, E., Behrens, C.J., Gross, M., Soreq, H., Heinemann, U., Friedman, A., 2008. Acetylcholine-induced seizure-like activity and modified cholinergic gene expression in chronically epileptic rats. Eur. J. Neurosci. 27, 965–975. https://doi.org/10.1111/j.1460-9568.2008.06070.x.

Zwierzyńska, E., Krupa-Burtnik, A., Pietrzak, B., 2017. The possibility of adverse effect of Kv7-channel opener retigabine on memory processes in rats. Epilepsy Behav. 75, 170–175. https://doi.org/10.1016/j.yebeh.2017.08.004.